CLRC

Technical Report
RAL-TR-97-008

Neutron Reflection Studies of Polymer-Polymer Interfaces

D G Bucknall and J S Higgins

January 1997

COUNCIL FOR THE CENTRAL LABORATORY OF THE RESEARCH COUNCILS

Enquiries about copyright, reproduction and requests for additional copies of this report should be addressed to:

The Central Laboratory of the Research Councils
Library and Information Services
Rutherford Appleton Laboratory
Chilton
Didcot
Oxfordshire
OX11 0QX
Tel: 01235 445384 Fax: 01235 446403
E-mail library@rl.ac.uk

ISSN 1358-6254

Neutron Reflection Studies of Polymer-Polymer Interfaces

DG Bucknall[§,*] and JS Higgins[‡]

§ ISIS Facility, Rutherford Appleton Laboratory, Chilton, OXON OX11 0QX
‡ Department of Chemical Engineering, Imperial College, London SW7 2BY

* To whom correspondence should be addressed

To be published in:

Recent Research Developments in Polymer Science

Ed H Hommell 1997

1. INTRODUCTION

Polymer interfaces and surfaces are an area of study that has always been important since they impinge on all aspects of polymer science. The interfacial behaviour is fundamental to the bulk properties of the system, and consequently the applications of the polymers. For instance adhesion, miscibility, compatibilisation, welding, surface wetting, blend morphology, mechanical strength, etc, are all controlled by interfacial behaviour. The characterisation and understanding of these properties on a microscopic level are therefore of vital importance.

Numerous techniques have been applied to investigate the surface and interfacial behaviour of polymers. However, the accuracy demanded of the experimental data in order to obtain useful interfacial information requires specialist techniques and the associated equipment that goes with them. One technique which has seen an explosion in popularity within the polymer community over the last ten years is specular neutron reflectivity. The reasons for this popularity are partly to do with the development and advances in the reflectometers, but are mostly associated with the simple fact that neutron reflectivity is often the only technique that can answer the questions that are being posed by the polymer interface community. The wealth of information that can be obtained by a well designed experiment would have been difficult to comprehend ten years ago. The object of this contribution is to demonstrate the power of the technique and why it is worth going to one of the handful of neutron sources around the world where neutron reflectometers are operated.

2. REFLECTIVITY TECHNIQUE

Neutron reflection provides the composition variation normal to the surface of the polymer film, with an accuracy on a sub-nanometer length scale. This kind of information is also given by X-ray reflectivity and to some degree also by light ellipsometry, however the neutron scores over these other radiation sources in two important respects. Firstly, there is the favourable difference in scattering properties between elements and isotopes of elements. With X-rays contrast between different regions of the sample is provided by the electron density difference between molecules, whilst for light it is the refractive index. The analogue for neutrons is the neutron scattering cross section. Across the periodic table, this scattering cross section appears to be not only of random magnitude, but also of sign and varies even between isotopes of a specific element. For the polymer scientist the neutron is of particular interest because hydrogen and deuterium have vastly different neutron cross sections. This means that with a little careful chemistry deuteration can open up a huge area of unique experimental possibilities. Deuteration is

therefore an ideal labelling technique to highlight whole molecules or specific sections of the polymer and produce a large contrast variation with the normal hydrogenous molecules around it.

The second major advantage is that the neutron can penetrate through many engineering materials. This allows the use of neutrons in complex sample environments if the situation warrants it, without the worry of absorption, which is a major problem for light and X-ray techniques. The energies of the thermal neutrons used for reflectivity, make the technique non-destructive, allowing repetitive measurements on one sample to be made, for instance to look at changes after successive annealing processes. The neutrons do not require high vacuum containment which allows samples to be measured under normal atmospheric conditions. Because of these advantages there should be little wonder at the huge growth in the application of neutron reflectivity to the investigation of polymer interfaces and surfaces. However, it must always be remembered that although neutron reflectivity is an extremely powerful technique, it should be used in conjunction with other techniques to fully exploit its potential.

3. REFLECTION THEORY

It is the wave behaviour of neutrons that has allowed a close analogy with classical optics. With only a few minor modifications, neutron waves are able to reflect, refract and interfere following all the standard optical rules [1]. A full discussion of the theory of reflection is not appropriate at this point since this has been covered extensively in the literature [1,2]. However, it is necessary to include a brief description of the essential points since an understanding of them is vital in the interpretation of reflectivity data.

At this point it is necessary to define a few concepts. An interface is defined as the position between media of 2 different refractive indices. The neutron refractive index of medium j is given as:

$$n_j = 1 - \frac{\lambda^2 N_d b}{2\pi} + \frac{i\lambda N_d \sigma_a}{4\pi} \qquad (1)$$

where N_d is the atomic number density, b is the coherent scattering length, the product $N_d b = \rho_s$ is the scattering length density, σ_a is the adsorption cross-section and λ is the neutron wavelength. Strictly then the refractive index is a complex number. For most materials, however, with the exception of those containing the elements, Li, B, Cd, Sm, or Gd, the adsorption cross-section is effectively zero, *i.e.* $\sigma_a \approx 0$, and therefore for most polymers Equation 1 reduces to:

$$n_j = 1 - \frac{\lambda^2 N_d b}{2\pi} = 1 - \frac{\lambda^2 \rho_s}{2\pi} \qquad (2)$$

The neutron scattering length b is a nuclear property describing the interaction between the neutron and the atomic nucleus [3]. The value of b varies randomly across the periodic table and also between isotopes of the same element [4]. Here neutrons present a big advantage over other radiation such as light or X-rays, with isotopic substitution providing enhanced contrast between two otherwise equivalent species. The large difference in b between ^{1}H and ^{2}H (D) is of particular usefulness to the polymer scientist, as will be discussed in a little more detail later.

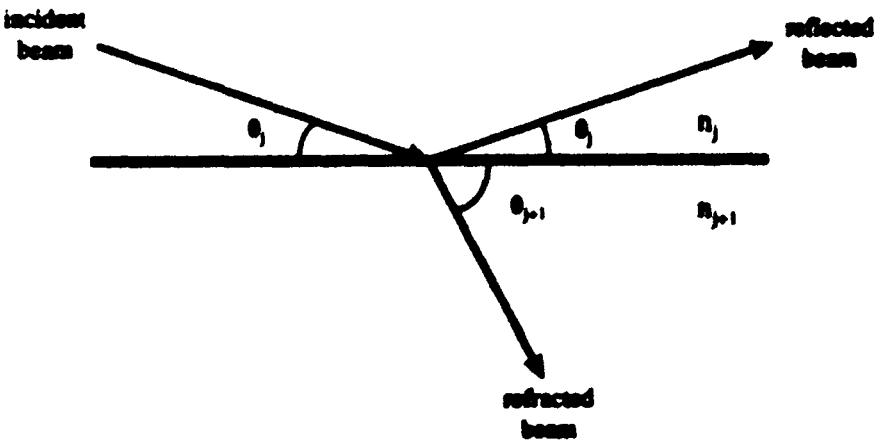

Figure 1: Schematic diagram of an incident neutron beam on a flat interface between two media, showing the reflected and refracted beams.

Figure 1 shows a neutron beam incident on an interface between two infinitely thick media with refractive indices n_j and n_{j+1}, where the interface is also infinitely sharp. The beam can

be either reflected, at an angle, θ_j, equal to that of the incident beam, or refracted with an angle according to Snell's Law [5]:

$$n_j \cos\theta_j = n_{j+1} \cos\theta_{j+1} \qquad (3)$$

Taking the case where the interface is between a vacuum, or essentially air, (j=0) and a liquid or solid (j+1=1), then n_0 is 1 and Equation 3 reduces to $\cos\theta_1 = n_1^{-1} \cos\theta_0$. At a critical angle, $\theta_0 = \theta_c$, the angle of refraction becomes zero ($\theta_1 = 0$) and thus $cos\theta_c = n_1$. For values of $\theta_0 < \theta_c$ total external reflection of the incident beam is observed with only an evanescent wave refracting into the sample. For values of $\theta_0 > \theta_c$ external reflection of the incident beam is accompanied by refraction into the sample.

The reflectivity of an incident beam on an infinitely sharp interface as described above is defined as the ratio of the reflected to incident beam energies [5]. A similar expression for the ratio of the refracted to incident beam energies defines the transmissivity, T. The reflectivity has both parallel and perpendicular components with respect to the interface. It is only the perpendicular reflectivity component that is of importance to the specular reflection of neutrons, since is contains the information about the concentration-depth profile.

The perpendicular reflectivity, R, is determined using the Fresnel reflection coefficient, $r_{j,j+1}$, for the interface described in Figure 1, which is defined:

$$r_{j,j+1} = \frac{n_j \sin\theta - n_{j+1} \sin\theta_{j+1}}{n_j \sin\theta + n_{j+1} \sin\theta_{j+1}} \qquad (4)$$

The reflectivity is then simply given by:

$$R = r_{j,j+1} r^{*}_{j,j+1} \qquad (5)$$

where the asterisk (*) denotes the complex conjugate. Since there is no complex component to the reflectivity from most materials then this simplifies to $R = r^2_{j,j+1}$. The reflectivity from this sharp interface is characterised by the critical angle, θ_c, indicated by the point at which the reflectivity drops from unity, and is often referred to as the critical edge. The wavelength at which this occurs is given by $\theta_c \approx \lambda(Nb/\pi)^{0.5}$. Since the neutron momentum transfer is related to the incident angle and wavelength by the relationship

$$q = 2k = \frac{4\pi}{\lambda} \sin\theta \qquad (6)$$

it is also possible to derive $r_{j,j+1}$ and hence R in terms of q. Therefore, the reflection coefficients are given by:

$$r_{j,j+1} = \left(\frac{q_{z,j} - q_{z,j+1}}{q_{z,j} + q_{z,j+1}} \right) \qquad (7)$$

where $q_{z,i}$ are the component of the momentum transfer perpendicular (normal) to the surface. Since $q_{z,i} = 2\left(q_z^2/4 - q_c^2/4\right)^{0.5}$, where q_z is defined by Equation 6, and q_c is the critical value of $q_{z,i}$ below which total reflection occurs. Substituting Equation 7 into Equation 5 gives the reflectivity for a sharp interface between two bulk media as:

$$R(q) = \left[\frac{1 - \left[1 - \left(q_c/q_z\right)^2\right]^{1/2}}{1 + \left[1 - \left(q_c/q_z\right)^2\right]^{1/2}} \right]^2 \qquad (8)$$

This is also known as the Fresnel reflectivity and is often denoted as R_f. A calculated Fresnel reflectivity is shown in Figure 2(a). The region of total reflection below q_c is clearly visible. The drop off in reflectivity at $q_z > q_c$ can be shown to be proportional to $1/q_z^4$, at large values of q_z [2, 6] which is identical to the behaviour observed in systems which have infinitely sharp interfaces and scattering that obeys Porod's Law.

One interesting result is that the plot of $R(q_z)q_z^4$ asymptotes to a limiting value which is proportional to the square of the reflectance at the air-media interface.

With these equations in mind, the problem of a sample containing m discrete layers can now be addressed. The situation is shown in Figure 3, where the $(m+1)$ layer is the substrate and 0 is

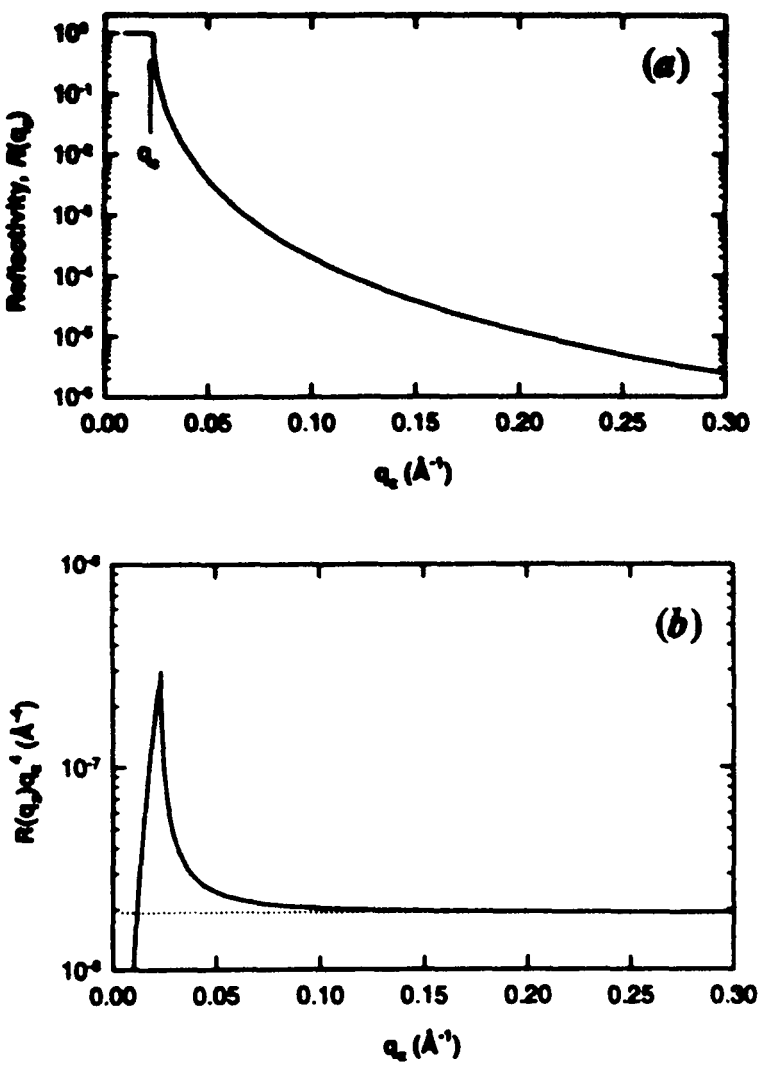

Figure 2: (a) Calculated Fresnel neutron reflectivity profile from an infinitely sharp interface between two media obtained from Equations 4 and 5 or 8. Total reflection ($R = 1$) occurs for $q_z \leq q_c$. (b) Reflectivity multiplied by q_z^4, showing the asymptotic limit reached at large values of q_z.

defined as the medium surrounding the sample, *i.e.* air. The reflection coefficient for the sample is calculated by firstly considering the coefficient between the substrate and the bottom layer, $r_{m,m+1}$, *i.e.* between the $(m+1)^{th}$ and m^{th} layers, which is simply given by Equation 4 where $j = m$. The reflectivity coefficient between the $(m\text{-}1)^{th}$ and m^{th} is then given by:

$$r'_{m-1,m} = \frac{r_{m-1,m} - r_{m,m+1}\exp(2i\beta_m)}{1 + r_{m-1,m}r_{m,m+1}\exp(2i\beta_m)} \qquad (9)$$

where $r_{m-1,m}$ is again given by Equation 4, and the prime (′) indicates that internal reflections have been taken into account, in this case between the m-1, m and m, m+1 interfaces. A phase factor, β_m, has also been introduced and represents an optical path length term for the mth layer, such that, $\beta_m = (2\pi/\lambda)n_m d_m \sin\theta$, where n_m and d_m are the refractive index and thickness

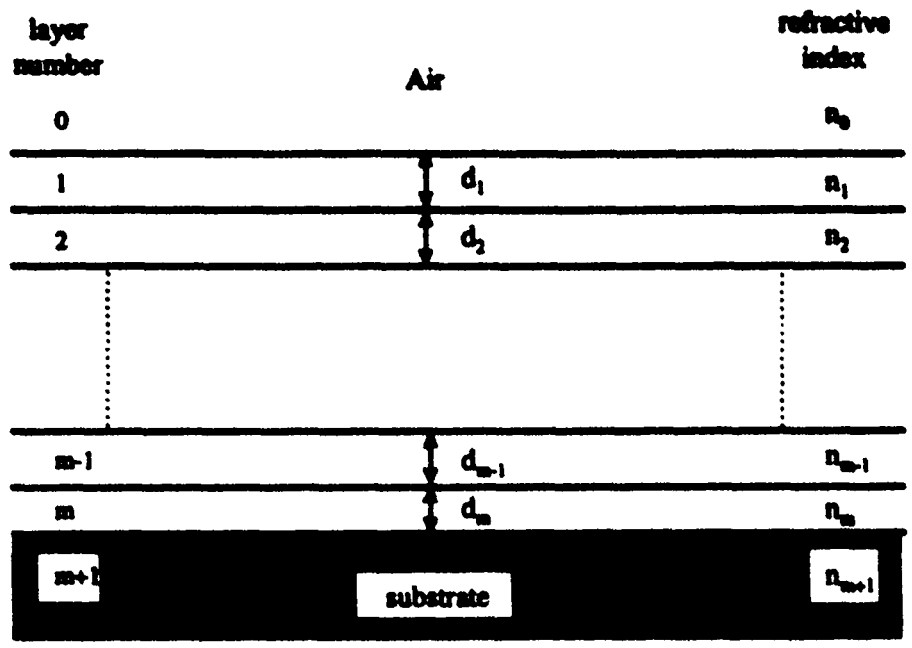

Figure 3: Schematic diagram of a sample composed of m discrete layers each with a thickness, d_i, and refractive index, n_i.

respectively of layer m, and θ is the angle of incidence. The reflectance, $r'_{m-2,m-1}$, is calculated in a similar way, and the process continued in a recursive method for each successive layer until the reflectivity coefficient for the top layer, $r'_{0,1}$, is obtained. The reflectivity, R, is then given by substituting $r'_{0,1}$ into Equation 5.

For a double layer sample Equation 9 can be applied together with Equation 5, to give the reflectivity profile shown in Figure 4(*a*) for a deuterated polystyrene (dPS) layer on a poly(methyl methacrylate) (PMMA) layer on a silicon substrate. The minima and maxima observed are characteristic of the layer thicknesses. When the neutron wavelength satisfies the Bragg condition $\lambda = 2d_i \sin\theta$, constructive interference occurs. This leads to $d_i = 2\pi/\Delta q_i$, where Δq_i is the difference between successive minima. Therefore the high frequency interference fringes are from the thicker layer, in this case 600 nm, and the low frequency fringes from the thinner layer of 200 nm thick. The reflectivity in the Rq^4 versus q plot as in Figure 4(*b*) is seen to asymptote to a limiting value at high q values, which is proportional to the sum of the squares of the reflectances at each of the interfaces, given by:

$$Rq_z^4 = 16\pi^2 \sum_{i,j} \left(\rho_i^2 - \rho_j^2\right) \qquad (10)$$

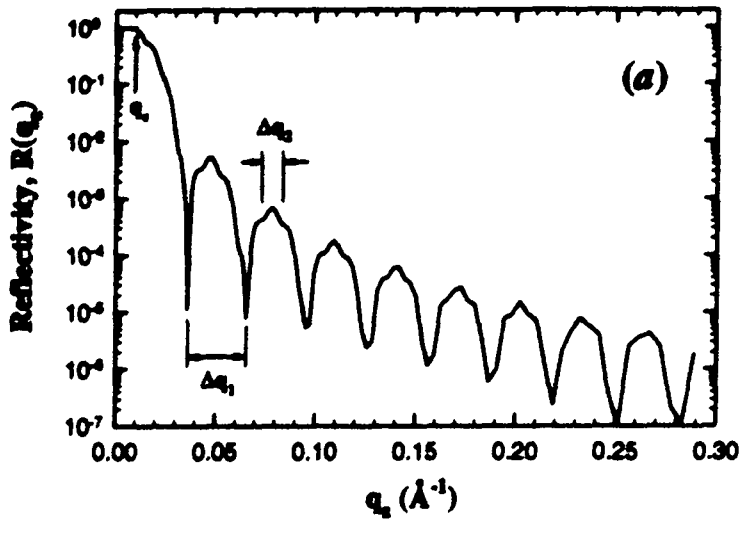

Figure 4: (*a*) Calculated reflectivity profile of a bilayer of dPS on PMMA on Si using Equation 5 and 9. (*b*) Reflectivity plotted as Rq^4 versus q, showing that the reflectivity oscillates about an asymptotic value (dashed line).

This approach to calculating reflectivity is exact, but extending it to multilayer systems proves to be extremely cumbersome mathematically. For this reason many people have favoured a more general solution and perhaps the most versatile and widely used among these is that of Abeles [7]. This method defines a characteristic matrix for each discrete layer so that for the *m*th layer the corresponding matrix is:

$$c_m = \begin{bmatrix} \cos\beta_m & -(i/\kappa_m)\sin\beta_m \\ -i\kappa_m \sin\beta_m & \cos\beta_m \end{bmatrix} \qquad (11)$$

where $\kappa_m = n_m sin\theta_m$ and β_{m-1} has been defined above. Once matrices for each individual layer have been calculated, an overall sample matrix M is defined as the product of the individual matrices, so that for a sample with m layers as described in Figure 3 the resultant matrix is defined as:

$$M = \prod_{m=0}^{m} c_m = \begin{bmatrix} M_{11} & M_{12} \\ M_{21} & M_{22} \end{bmatrix} \qquad (12)$$

The reflectivity is then simply related to the matrix elements from M by the relationship:

$$R = \left| \frac{(M_{11} + M_{12}\kappa_{m+1})\kappa_0 - (M_{21} + M_{22})\kappa_{m+1}}{(M_{11} + M_{12}\kappa_{m+1})\kappa_0 + (M_{21} + M_{22})\kappa_{m+1}} \right|^2 \qquad (13)$$

where m+1 denotes the substrate and 0 the air. As can be seen this general solution lends itself very well to the use of computers. It is well suited to modelling the reflectivity profiles from samples with complex internal layer structure.

4. INSTRUMENTATION

It is obvious from the definition of the momentum transfer q (Equation 6) that reflectivity measurements as a function of q can be achieved by varying either θ or λ. Fixed wavelength reactor sources using monochromatic beams therefore vary θ to give the required q range, whereas pulsed neutron sources use a broad band or 'white' beam polychromatic beam and time-of-flight (TOF) to determine λ at fixed θ. Common to both methods of measurement however is a high degree of automation which is essential for accurate measurement of $R(q)$. Perhaps the major drawback to neutron reflectivity is the limited number of instruments around the world, which basically only reflects the small number of facilities. However, the number of instruments continues to grow.

This article is not meant to be a comprehensive review of instruments since this has been dealt with in depth in the literature (see for example References 8-17 with a good review by Russell [6]). With two ways of producing neutrons there are basically two designs of reflectometer, each of which will be illustrated by describing typical instruments.

The CRISP reflectometer at the ISIS Facility at the Rutherford Appleton Laboratory is typical of

a pulsed source time-of-flight (TOF) instrument. A schematic illustration of the major optical components is shown in Figure 5. The moderated neutrons pass through a double set of choppers, firstly, a disc chopper to select the wavelength range and then a prompt pulse suppressing nimonic chopper. The beam is coarsely collimated by neutron absorbing jaws before entering the experimental measurement area. Fine collimation is achieved by two slits before the sample which define the illuminated area and resolution at the sample position. The beam profile and intensity is monitored just before reaching the sample using a scintillator detector. Post sample the background noise is suppressed by two further slits or by a shielded nose cone. Reflection is detected either with a single or a position sensitive detector. CRISP views a liquid hydrogen moderator which gives a wavelength range of 0.5-6.5 Å, with the disc chopper working at 50 Hz. This range can be extended to 12 Å if the disc chopper is operated at 25 Hz, although this has the drawback of only collecting 1 in every 2 pulses of neutrons. The instrument has been designed to be able to measure liquid surfaces and therefore has a horizontal sample geometry and an inclined beam at 1.5° to the horizontal. At 50 Hz this angle yields a q_z range of 0.05 to 0.65 $Å^{-1}$, which is optimised for liquid surface measurements. In this q region the kinematic approximation (see Section 6) is applicable and is widely utilised for analysis of monolayer structure at the air-water interface [18]. Computer controlled goniometers at the sample position allow movement of solid samples (or confined liquids) to angles other than the 1.5° specified by the instrument design geometry. For liquid surfaces accessing angles less than 1.5° to measure in a q range lower than 0.05 $Å^{-1}$, a super-mirror is inserted in the path of the beam. This super-mirror totally reflects all wavelengths greater that ~1.5 Å, and reduces the angle of incidence on the sample by $\theta = 1.5 - \theta_{sm}$ where θ_{sm} is the angle of the super-mirror to the beam. CRISP like other pulsed neutron source reflectometers has a fixed wavelength range, therefore at each incident angle on the sample a limited q range is obtained. The q range can easily be extended by running 2 or more incident angles and combining the data [9]. The reflectivity profile at a fixed incident angle due to the polychromatic beam is therefore collected all at once, and the time required to measure the total spectrum is only limited by the statistics of the collected data.

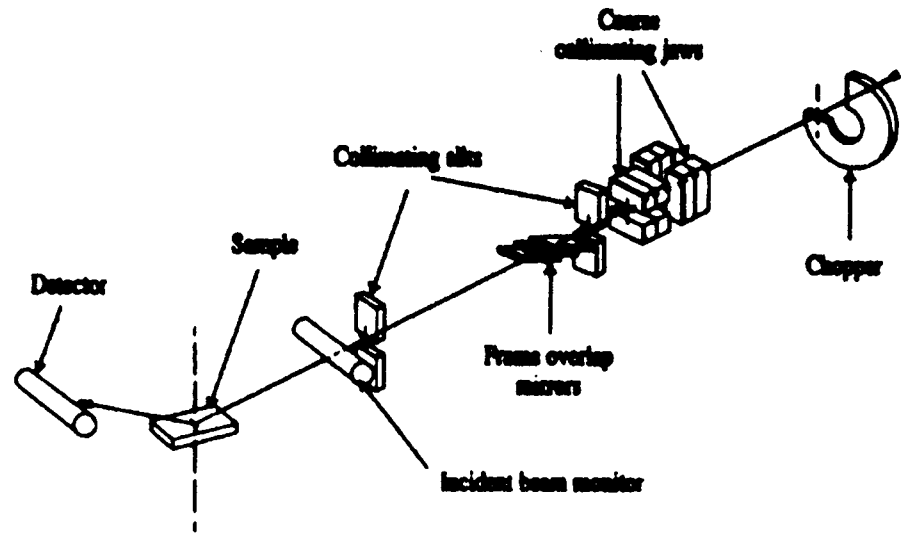

Figure 5: Schematic layout of the time-of-flight neutron reflectometer CRISP at the ISIS Facility, Rutherford Appleton Laboratory.

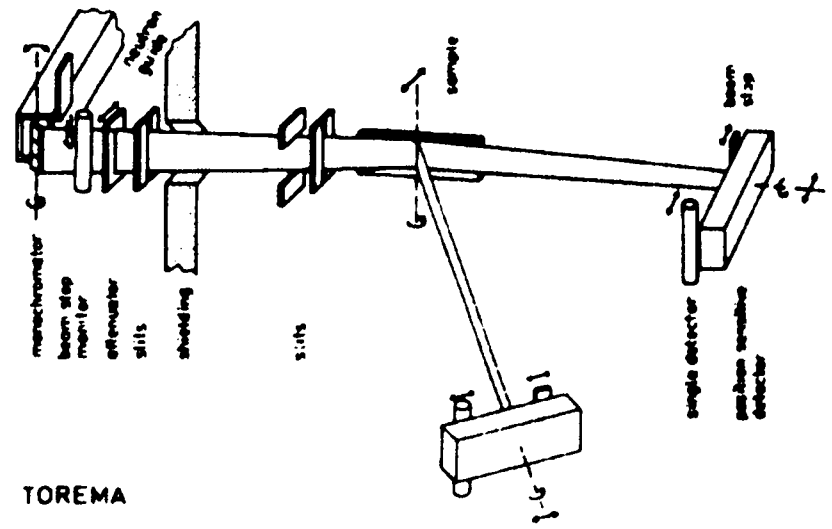

Figure 6: Schematic of the fixed wavelength neutron reflectometer Torema II at the GKSS.

By contrast reactor based reflectometers with fixed wavelength sources measure the reflectivity profile point-by-point in θ and hence in q. This method of measurement is often called θ-2θ scans and is identical to the method employed by the closely related X-ray reflectometers. A typical example of a θ-2θ neutron reflectometer is Torema II at the GKSS research reactor, Hamburg, Germany (see Figure 6). Here moderated neutrons are focused using a monochromating graphite crystal to give a neutron wavelength of 0.43 nm. The beam flux

is then monitored before attenuation and 3 variable slits define the beam on the sample. The sample is vertically mounted and is rotated at each angle of measurement (θ). The position sensitive detector is rotated at each measurement point at twice the incident angle (2θ). Due to the relatively high neutron flux at reactor sources , it is necessary at the lower incidence angles to attenuate the beam using plexiglass plates before the collimation to reduce the intensity reaching the sensitive detectors. A drawback of this technique is that both sample and detector must move with respect to the beam. This has a serious repercussion in that the illuminated area varies with rotation of the sample. This is not a problem if there are no lateral inhomogeneities, but can pose difficulties for data interpretation of the measured reflectivity profile if they do exist. On the whole, many of the advantages or disadvantages regarding sample measurement are trivial and the real differences between instruments now seems to be the perception by the users as to speed of measurement. This is only related to the 'brightness' of the neutron source and not the reflectometer.

5. ISOTOPIC SUBSTITUTION

As mentioned before, one of the greatest assets available to neutron reflectivity and of course neutron scattering in general is the use of isotopic substitution for contrast enhancement. For the polymer scientist this is extremely important, because by substituting hydrogen for deuterium a vastly different scattering length density can be produced. This has enormous implications since by a very minor chemical alteration it is possible to contrast a molecule or even a part of a molecule from an environment. In Table 1 the scattering length densities for some common polymers are compared in their normal hydrogenous and deuterated forms using the equation:

$$\rho_z = \frac{\sum b_i D_m N_A}{M_m} \qquad (14)$$

where $\sum b_i$ is the sum of the monomer atomic coherent scattering lengths, [4] D_m is the bulk polymer density, N_A is the Avogadro constant and M_m is the monomer molar mass. The use of deuteration can be illustrated further by imagining a reflectivity experiment, for example polymer-polymer interdiffusion, where it is not possible to distinguish between the polymers using X-rays. If two different polymers are chosen their hydrogenous isotopic forms may have enough natural contrast to distinguish between them using neutrons. By comparison of the values in Table 1, however, it is seen that even in this case the differences are very small. Consider now the case of interdiffusion between layers of the same polymer, something which is of vital interest in all aspects of adhesion for example. Here there is no natural contrast and indeed the separate layers are totally identical and no distinction between the sample before and after annealing can be made. If however, one layer is made of deuterated polymer a large difference is immediately introduced between it and the normal hydrogenous layer. When the layers interdiffuse the change in the interface from a sharp step to a diffuse profile can easily be followed. This deuteration scheme can also

Table 1: Calculated bulk scattering length density values for some common polymers in both their hydrogenous and deuterated forms, calculated using Equation 14.

Polymer	Abbreviation	ρ_z (Å^{-2}) × 10^6	
		hydrogenated	deuterated
polystyrene	PS	+1.41	+6.50
poly(methyl methacrylate)	PMMA	+1.10	+7.22
polyethylene	PE	-0.33	+8.24
poly(dimethylsiloxane)	PDMS	+0.06	+5.04
polybutadiene	PB	+0.41	+6.60

be applied to enhance the natural contrast between layers of two different species. Indeed it can be used in a whole host of experiments for example to look at molecules segregating to interfaces and surfaces, or even deuterating the ends of polymer chains to look at preferential adsorption. The use of such deuterated contrast enhancement seem endless and only limited by the ability of the synthetic chemists who provide the labelled polymers.

However, a cautionary note must be added. Although for the most part deuteration leaves a polymer with physically identical properties, for a few well studied examples deuteration can alter considerably the polymer behaviour, especially near phase transitions. Blends of some polymers have been shown to display upper critical solution temperatures contradicting the expected assumption that such isotopic blends form ideal mixtures [19-30]. The effect was first noted for isotopic mixtures of hydrocarbons [31], but has been observed for polystyrene (PS) [19, 22, 23, 26] polybutadiene (PB) [20] and poly(ethylenepropylene) (PEP) [25]. When annealed to equilibrium thin films of isotopic blends of these polymers have a non-homogeneous structure with the lower surface energy component preferentially segregating to the air-polymer and polymer-substrate interfaces. The segregation occurs due to a weakly unfavourable χ interaction parameter originating from the difference in polarizability between C-H and C-D bonds [22]. The effect is only observed however, if the relationship:

$$\chi < \frac{2}{N} \qquad (15)$$

is satisfied, where N is the degree of polymerisation. This means that isotopic segregation in these system is only evident if $N > 2/\chi$ and since χ is typically very small for hydrogenous-deuterated mixtures (χ(h/d-PS) $\approx 2\times10^{-4}$ [20]) means that effectively N must be very large. Although this segregation may in principle be a problem in practice it is not so, since careful use of deuteration and design of the experiment can eliminate the problem entirely.

6. DATA ANALYSIS

Routine analysis of reflectivity data would ideally be solved by direct inversion of experimental data into either scattering length density, $\rho(z)$, or even volume fraction, $\phi(z)$, profiles. Generally, this cannot be achieved due to the loss of phase information, making this closely related to the phaseless Fourier problem [32]. The analysis then becomes effectively the reverse situation, where reflectivities calculated from simulated $\rho(z)$ profiles are used in a comparative way to minimise deviations from the measured reflectivity.

For simple systems analytical expressions exist for calculating reflectivity profiles, using the relationships of Fresnel and Snell (see above). However, most real samples do not typically conform to this simplistic ideal. Extracting the scattering length density profile from the reflectivity data, $\boldsymbol{R}(q)$, becomes necessarily more complex. Because of the lack of phase information from measured reflectivity data it is not generally possible to directly obtain $\rho(z)$ profiles by inversion of the $\boldsymbol{R}(q)$ curve. Analysis of the $\boldsymbol{R}(q)$ curves to give $\rho(z)$ profiles is generally not unique in that it is possible that several different $\rho(z)$ profiles are consistent with the experimental data given the experimental error and limited q range. There are essentially two methods of data analysis:

- model fitting
- approximations and free-form techniques.

These are briefly described below together with a review of theoretical work on inversion techniques which are still not widely applicable to real problems due to the limitation with regard to the lack of phase information.

It should be stressed that many of the problems associated with fitting reflectivity data such as uniqueness of fit can be alleviated by use of complementary techniques. In cases where such additional information is not available the careful design of the experiment becomes imperative, and labelling schemes must be extensively used. In general the more information acquired regarding the sample the easier the task of fitting the data.

6.1 Model Fitting

The standard approach to reflectivity analysis is model fitting and refinement mostly using the matrix technique. In this method a functional form for $\rho(z)$ is chosen on the basis of all known data about the system. This will include any complementary information from other reflectivity measurements and/or techniques. The resulting reflectivity profile assuming the $\rho(z)$ model is computed using Equations 11, 12 & 13 and compared to the experimental data. The parameters of the model are then modified using least-squares or simplex fitting routines so that the deviations of the calculated and measured reflectivity profiles are minimised [33]. Clearly then this approach requires a significant amount of prior knowledge of the sample. This method works well when the system is quite well defined and therefore the initial model $\rho(z)$ profile gives $\boldsymbol{R}(q)$ sufficiently close to the experimental data. This approach has the advantage that many of the other non-unique solutions for $\rho(z)$ can be eliminated based on the expected physical properties of the system. However, many cases present themselves where no reasonable starting guess for $\rho(z)$ exists, making the process of model fitting one of hard work and many intuitive guesses.

All the equations so far used to describe the reflectivity from specimens have been from infinitely sharp interfaces. However, no interface is infinitely sharp, but exhibits a gradient in density not only between the specimen and the surrounding media, i.e. the substrate or air, but also between consecutive layers of polymers. This may represent a diffuse interface between the polymers or even interfacial roughness or waviness. It is important to distinguish between these. Extensive treatment of interfacial roughness and waviness can be found in the literature [34-36]. The difference between roughness and waviness is evident in the $\rho(z)$ profile projection over the neutron coherent length, l_c [6]. Long-range roughness or waviness of the interface over distances larger than, l_c, has an effect similar to that of a divergence of the incident beam. This can be seen as leading to a small curvature in the $\rho(z)$ profile. Neutrons impinging on a rough interface, with interfacial

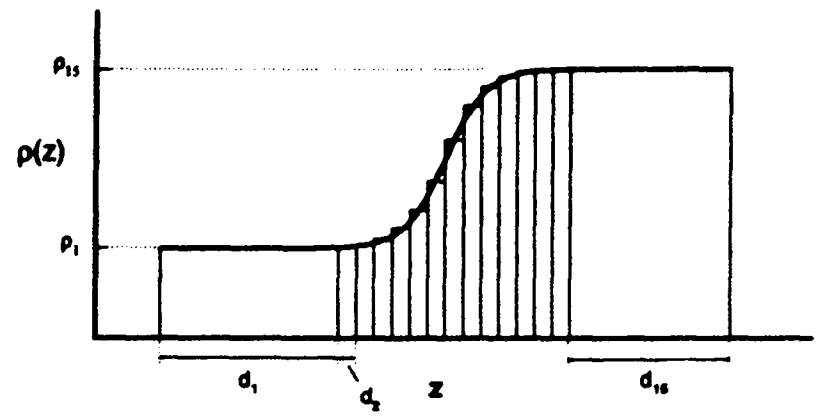

Figure 7: Schematic diagram to show how a diffuse interface, in this case a hyperbolic tangent function, between two polymers can be described by division of the system into histograms with discrete thicknesses, d_i, Associated with each layer is a specific scattering length density, ρ_i.

waviness smaller than l_c, have local angles of incident which vary greatly from the average. When projected onto a $\rho(z)$ profile this gives a wider smooth transition between the two layers. In general, this leads to a reduction in the reflectivity arising from that interface. Névot and Crocé [37] showed that for a Gaussian roughness at a bulk interface the Fresnel reflectivity is modified by an exponential factor:

$$\boldsymbol{R} = \boldsymbol{R}_f \exp\left(-\boldsymbol{q}^2\sigma^2\right) \qquad (16)$$

where σ is the standard deviation of the Gaussian function describing the roughness. Clearly, from this equation it can be seen that reflectivity is very sensitive to interfacial roughnesses. Large deviations from Fresnel reflectivity are expected even for small amounts of roughness. The treatment of roughness has been extended to thin layers by applying a similar Gaussian factor to the reflectivity coefficients of Equation 7 [38]:

$$\boldsymbol{r}_{ij} = \left(\frac{\boldsymbol{q}_{z,j} - \boldsymbol{q}_{z,j+1}}{\boldsymbol{q}_{z,j} + \boldsymbol{q}_{z,j+1}}\right)\exp\left(-\frac{\boldsymbol{q}^2}{2}\sigma^2\right) \qquad (17)$$

An alternative approach to introducing a diffuse interface between two bulk layers is to divide the interface into a number of discrete layers as shown in Figure 7. The change in concentration between each layer must be small enough that the calculated reflectivity profiles do not contain

interference fringes associated with the arbitrary choice of histogram thicknesses.

6.2 Maximum Entropy and Bayesian Analysis

Since generally the total thickness of the sample is known from other techniques it is possible to apply a free form solution. One approach is the simulated annealing procedure [39], where the total sample thickness is divided into a suitably large number of equally sized pixels. The problem then becomes one of statistically varying the values of ρ_z in each pixel with certain restrictions concerning jump height and smoothness of curve. This method has the advantage that very little is assumed about the nature of the density profile. However, it does suffer from ambiguity since it is possible to produce a large number of satisfactory fits which are quite possibly meaningless. This problem can be reduced if a suitable starting situation is used. An alternative approach which has been gaining much interest and demonstrated considerable success especially among the polymer community is the maximum entropy (MaxEnt) technique of free form solutions [32, 40, 41]. This uses entropy as a regularising function when varying the value of ρ_z in each of the pixels, which make up the model. A smoothing correlation function is applied to the values of ρ_z between pixels removing physically meaningless small wavelength ρ_z spikes which could occur with uncorrelated pixels. Codes now exists where very little prior knowledge is required other than total sample layer thickness and air and substrate scattering length densities. The program developed by Sivia [42] tries to fit at first one layer and then incrementally more layers to a $\rho(z)$ model until a precision limit is reached in a χ^2 fit of calculated and experimental $R(q)$. Clearly then these free-form solutions can prove very useful in interpreting data, but a cautionary note must be added that some of the results may still be meaningless.

From the reflectivity data, R(q) it is desired that the scattering length density profile, $\rho(z)$, can be inferred. This inference can be summarised mathematically by the conditional probability distribution function (PDF), $\text{prob}[\rho(z) \mid R(q)]$, [32] where '|' means given. This means that with respect to the data, the best estimate of R(q) is given by the $\rho(z)$ profile which maximises this PDF.

However, this PDF is an unknown, and to calculate it, it is necessary to apply Bayes' Theorem. Bayes' Theorem relates the unknown PDF to two others, one of which can be calculated and the other estimated.

$$\text{prob}[\rho(z) \mid R(q)] \propto \text{prob}[R(q) \mid \rho(z)] \times \text{prob}[\rho(z)] \qquad (18)$$

Using Bayesian terminology the 'prior' PDF ($\text{prob}[\rho(z)]$) represents the state of knowledge about $\rho(z)$ before measurement of the sample. The prior state of knowledge is that modified by the data through a 'likelihood function' ($\text{prob}[R(q) \mid \rho(z)]$), which indicates how likely it is that the data set would have been obtained given a trial $\rho(z)$ profile. To give the required PDF, called the 'posterior' PDF, the product of these 'prior' and 'likelihood' PDF's are taken. This then represents the state of knowledge about the density profile after data have been collected.

It is unusual to be totally ignorant of prior knowledge about the sample, since information is usually available on the sample preparation, in addition to the possibility of being able to describe the $\rho(z)$ profile by a histogram-like structure of 'heights' and 'widths'. This additional prior knowledge allows the problem to be simplified further, and an estimate of the $\rho(z)$ profile is then obtained by maximising the 'posterior' PDF, $\text{prob}[\{d_i, \rho_i\} \mid R(q), \rho_s]$, where d_i and ρ_i are thicknesses and scattering length densities of each of the M layers describing $\rho(z)$, and ρ_s is the substrate scattering length density. If the number of layers is known this is then a simple problem then of parameter estimation. If however, M is not known it is necessary to calculate the PDF $\text{prob}[M \mid R(q), \rho_s]$ [32, 40].

6.3 Speckle Holography and Other Techniques

Although the application of neutrons to the study of density profiles as a function of depth is now well established, the information obtained is

often subject to questions of uniqueness. In fact it is quite possible that several different models adequately describe the same reflectivity profile. The experimental data hold vital information about layer thicknesses as well as interfacial and surface structure. As described above most work to date has involved fitting paramaterised models to the measured data. This is mostly successful, but can lead to the possibility of scientific prejudice leading to constraints of the model. To alleviate this problem, the ability to directly invert the reflectivity data to a density-depth profile would be most desirable. However, the lack of phase information in the reflectivity data prevents true inversion, and while several inversion methods can be applied they still rely on some knowledge of phase information. This is discussed in more detail in section 6.4. Two related approaches to reduce ambiguity of fits, speckle holography and use of magnetic substrates, are briefly described below.

To alleviate the ambiguity problems inherent in traditional reflectivity measurements, a novel approach is based on the holographic speckle imaging technique [43, 44] used in optical astronomy, which Sivia [32, 45] has called speckle holography. Assuming that the reflectivity is related to the derivative of the density profile ($d\rho/dz$) by a phaseless Fourier transform:

$$R(q) = \frac{(4\pi)^2}{q^4}\left|\int_{-\infty}^{+\infty} \frac{d\rho}{dz} e^{iqz}\, dz\right|^2 \qquad (19)$$

then the autocorrelation function (ACF) of $d\rho/dz$ is given by the Fourier transform of $R(q)q^4$:

$$ACF\left(\frac{d\rho}{dz}\right) = c\int_{-\infty}^{+\infty} R(q)q^4\, e^{-iqz} dq \qquad (20)$$

where c is a constant. However, Sivia shows [32, 45] that autocorrelation functions are not unique unless there is a distant reference signal (see Figure 8). Such a reference signal can be introduced into a reflectivity sample by introducing a thick buffer layer between the real sample under investigation and the substrate. The $\rho(z)$ discontinuity at the substrate-buffer layer interface then acts as the distant reference in the $d\rho/dz$ plot. In practice, the reflectivity data plotted as Rq^4 versus q is Fourier transformed to give the autocorrelation function of $d\rho/dz$. The $\rho(z)$ profile is then simply obtained by integration of the peaks in the ACF($d\rho/dz$) profile. Although the Fourier approximation of Equation 19 is only strictly valid for $R(q) \ll 1$ and $q \gg q_c$, this method at least in principle should distinguish between previously ambiguous solutions.

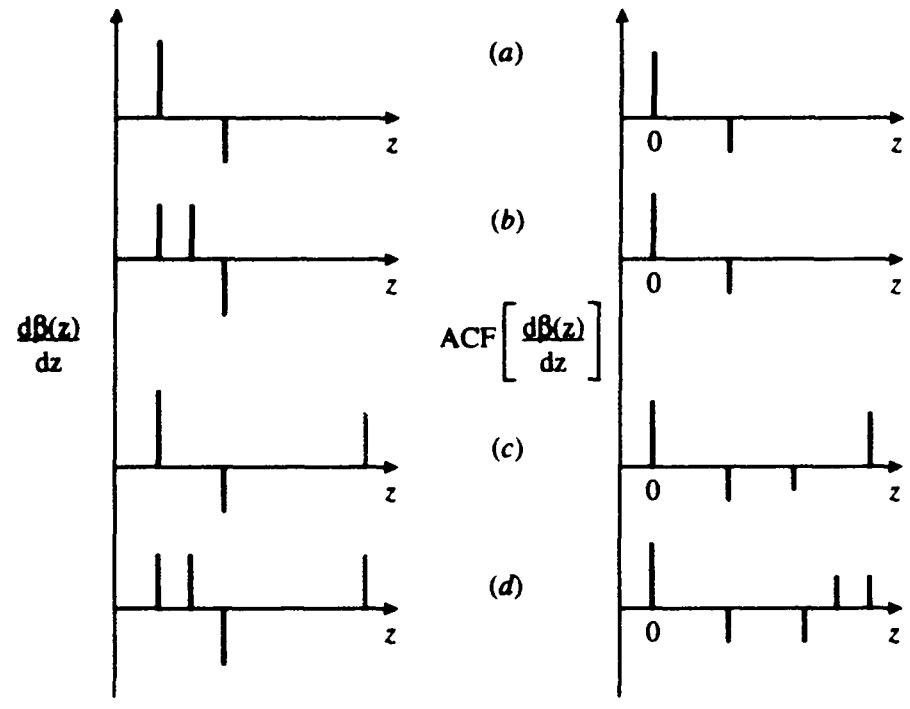

Figure 8: Derivatives of the scattering length density profiles ($d\beta/dz$) from 4 different samples, together with their autocorrelation functions (ACF($d\beta/dz$)). The values of $d\beta/dz$ in (*a*) and (*c*) and (*b*) and (*d*) are identical except for the inclusion of a reference point source on the right-hand side of (*c*) and (*d*). The inclusion of the reference source produces a scaled mirrored copy of the $d\beta/dz$ on the right-hand side of the ACF's (After References [32] and [45]).

Direct inversion of simulated data has shown that simultaneous use of X-ray and neutron reflectivity data on a sample with an additional artificial bilayer between the substrate and the film under investigation [46], can often eliminate ambiguities in data inversion [32]. This idea has been developed by Sanyal [47] for use with tuneable X-rays and the distorted-wave Born Approximation to successfully analyse

synchrotron reflectivity data obtained from Langmuir-Blodgett films. The neutron equivalent has also been developed and is based on the use of polarised neutrons and magnetised substrates, to determine uniquely and unambiguously the density profile of thin non-magnetic films [48].

The essential requirement of this technique is to be able to measure the unknown non-magnetic film on two different substrates whose scattering-length densities can denoted by ρ_1 andρ_2. Using a magnetised substrate and polarised neutrons this condition is satisfied for the scattering-length densities of the parallel and anti-parallel spin components of the polarised neutrons. In this way two simultaneous experiments are being performed on the same film but effectively different substrates. The scattering-length densities of the magnetic substrate will then be given by either the sum or difference of the nuclear and magnetic components. Under these conditions the difference in the reflectivities for the two neutron spin states is given by:

$$\frac{\left(R_1(q)-R_2(q)\right)}{R(q)} = \left(\rho_1^2-\rho_2^2\right)+ 2\left(\rho_1-\rho_2\right)\mathrm{Re}\left[\int \frac{d\rho(z)}{dz} e^{iq'z} dz\right] \quad (21)$$

Where z is the perpendicular distance to the surface, $R_i(q)$ are the reflectivities as a function of the neutron wavevector transfer, q, of the two spin states of the neutrons ($i=1,2$) and Fresnel reflectivity ($i=f$) and q' is the average wavevector transfer measured in the film. In the simplest approximation $R_f(q)$ is given by $4\pi/q^4$. If Equation (21) is Fourier transformed, the derivative of the scattering length density, $d\rho(z)/dz$, of the film is obtained directly and unambiguously:

$$\frac{1}{2\pi}\int\left(\frac{\left(R_1(q)-R_2(q)\right)}{R_f(q)}\right)e^{-iq'z}dz = \left(\rho_1-\rho_2\right)\delta(0) + \left(\rho_1-\rho_2\right)\left[\frac{d\rho(z)}{dz}+\frac{d\rho(-z)}{dz}\right] \quad (22)$$

The delta function, $\delta(0)$, arises from the interface between a substrate and the film deposited on it. Using polarised neutrons the reflectivities of $R_1(q)$ and $R_2(q)$ are obtained from the two spin states of the neutron when the sample is in a magnetic field. This technique is ideally suited to the study of polymer films, and preliminary experiments to demonstrate its effectiveness have been successfully demonstrated using a nickel substrate to determine the profile of a single dPS film, see Figure 9 [49]. Of course the technique is not restricted to single layers as demonstrated by the simulations of Sivia [48]. This study showed,

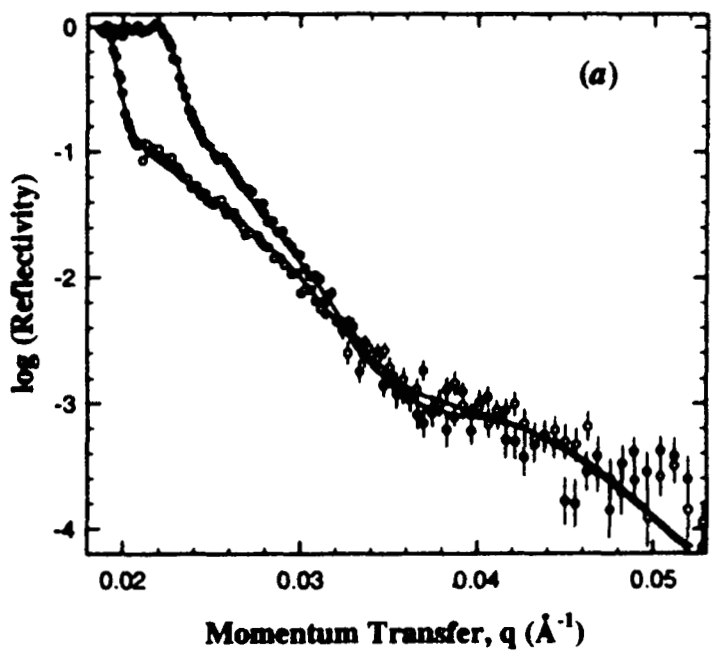

Figure 9: (*a*) Reflectivity curves of a dPS film on a nickel substrate measured using polarised neutrons with spins parallel (solid circles) and anti-parallel (open circles) to the magnetic field. (*b*) Autocorrelation function (ACF) data obtained by applying Equation 22 to the data of (*a*). The spike in the data at a z = 25 nm represents the thickness of the film.

however, that a perfectly sharp interface between the magnetic substrate and the non-magnetic film under investigation is vital for the distorted-wave Born Approximation to be valid.

6.4 Inversion Techniques

The ideal situation for analysis of reflectivity data would be a direct inversion of the experimental data into a $\rho(z)$ profile. However, a big obstacle to this becoming routine is the loss of phase information incurred due to the square term in the reflectivity coefficients $R(q)=|r_{01}|^2$. Due to this, there are presently no valid analytic expressions relating $R(q)$ to $\rho(z)$ over the entire q_z range of the reflectivity curve. However, in a limited number of cases direct inversion is possible. The kinematic approximation for example together with extensive deuteration schemes is very powerful for systems within the kinematic regime, i.e. in the limit of high q ($q>>q_c$) and which are weakly reflecting ($R>>1$). This limits the approach to systems which form very thin layers at bulk interfaces. The technique is well established therefore for the interpretation of reflectivity data of surfactants at the air-water interface (see for example references 18, 50, 51). The kinematic approximation has been applied to polymers adsorbed at the air-water interface [52] but is of limited use to most polymer systems.

True inversion as stated requires knowledge of not only the amplitude but also phase of the reflection coefficients, r_{01}. If these were known then in principle inversion of $R(q)$ into $\rho(z)$ profiles would be possible and practical algorithms exist. [53, 54]. However, in general, except in the cases discussed above, no phase information exists and methods to retrieve it from the measured reflectivity have been discussed on model simulated data in the literature [55-66]. However, many of these methods can yield numerous solutions for the phase, which then leads to non-unique inversion solutions. Extra data are then required to identify the correct solution, either by complementary depth profiling techniques [67, 68], or isotopic substitution methods [50, 51]. As seen above when placed on a magnetic reference substrate the reflectivity data from an unknown film which is non-magnetic can be inverted to $\rho(z)$ with the use of polarised neutrons. Schemes for inverting the two spin states of the reflectivity data have been proposed by Sivia [48] and Majkrzak [69]. However these methods are based on the Born approximation which is valid only in the kinematic limit ($q>>q_c$). Independently de Haan [70] and Majkrzak [65, 71] both proposed essentially identical methods for retrieving exactly the amplitude and phase information of the reflection coefficient even in the dynamic regime $q \approx q_c$. This method uses a 'tuneable' reference layer beneath the unknown layer. The complex reflection coefficient of the unknown layer can be obtained unambiguously by measuring the sample with 3 spin states with respect to the magnetic reference layer [66].

7. REFLECTIVITY STUDIES

Since neutron reflectivity was first used to study polymer thin films [72] the technique has been applied to an ever expanding field of polymer science. The unprecedented depth resolution has provided answers to problems not previously obtainable by other techniques. This ability to determine concentration gradients on the sub-molecular level has led to the rapid exploitation of the technique by the polymer community. A comprehensive review of all the applications to which neutron reflectivity has been applied would fill a book of its own, so this work limits itself to polymers at interfaces. Although this work is as up to date as the literature permits, the study of polymers with neutron reflectivity is never static and new work is continuously appearing. This article concentrates on studies which demonstrate particular aspects of neutron reflectivity, which are answering some of the fundamental questions of polymers interfaces.

7.1 Immiscible Polymer Interfaces

Use of blends containing immiscible polymers are widespread. Despite this there are limited numbers of experimental studies which examine the microscopic interfacial properties. The narrow interfacial widths which are characteristic of such blends are difficult to measure experimentally using conventional methods, and have lead to a wide scatter of

interfacial properties being reported in the literature. NR however, is ideally suited to looking at these interfacial problems with resolution of the order 0.1 nm even for buried interfaces. The parameters defining an interface between two polymers (*1* and *2*) used throughout this article are illustrated schematically in Figure 10.

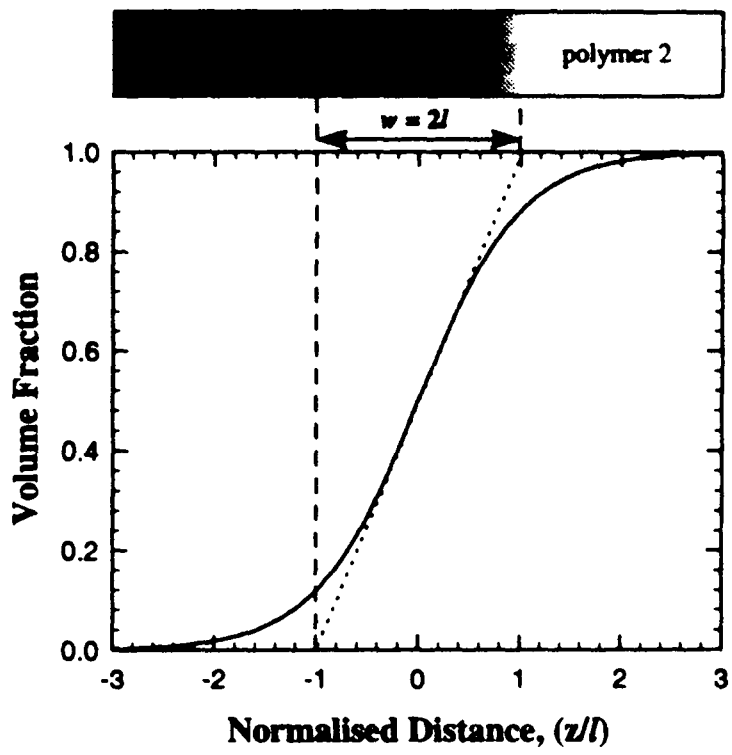

Figure 10: Schematic representation of interface defined by a hyperbolic tangent function [73] as described in the text.

One of the most extensively studied immiscible blend systems is polystyrene (PS) and poly(methyl methacrylate) (PMMA). In many ways this is a model system due to the similarity in physical properties between the two polymers. The glass transition temperatures, T_g, densities and statistical segment lengths, *a*, for both polymers are very similar [75]. Fernandez *et al* [74] studied the system of PS and dPMMA (where the d indicates deuterated) on highly polished quartz substrates. Measurements of a single PS layer and also a bilayer of PS and dPMMA on quartz were made. In both instances the samples were made by spin casting the PS directly onto the quartz substrate from dilute toluene solutions. The capping dPMMA was spin coated onto a separate glass slide and floated onto the dried PS film from the surface of water. This method of solvent casting is a standard approach for producing smooth, flat thin polymer films. The air-film roughness, of the single 800nm PS film was measured at 2.0nm. The interface between the PS and a 20 nm thick dPMMA layer was analysed by fitting both with a Gaussian roughness and an exponential density gradient. The interfacial roughness, σ, was found to remain at 2 nm even after annealing the system above the T_g of both polymers (see Figure 11). If interdiffusion occurred it was on a length scale below the instrumental resolution. This gives an upper limit for the interdiffusion of the dPMMA-PS blend at 120C of less than 2 ± 0.5 nm. From the change in the interfacial roughness the diffusion coefficient for this polymer pair D $\left(=\left(\Delta x/2\right)^2/4t\right)$ was evaluated as $< 3.62 \times 10^{-21}$ cm^2s^{-1} at 120C. Anastasiadis *et al* [16] have also measured the d-PS-PMMA interfacial width, *w*, using a bilayer of these polymers on a Si single crystal substrate, where:

$$w = 2l = (2\pi)^{1/2}\sigma \qquad (23)$$

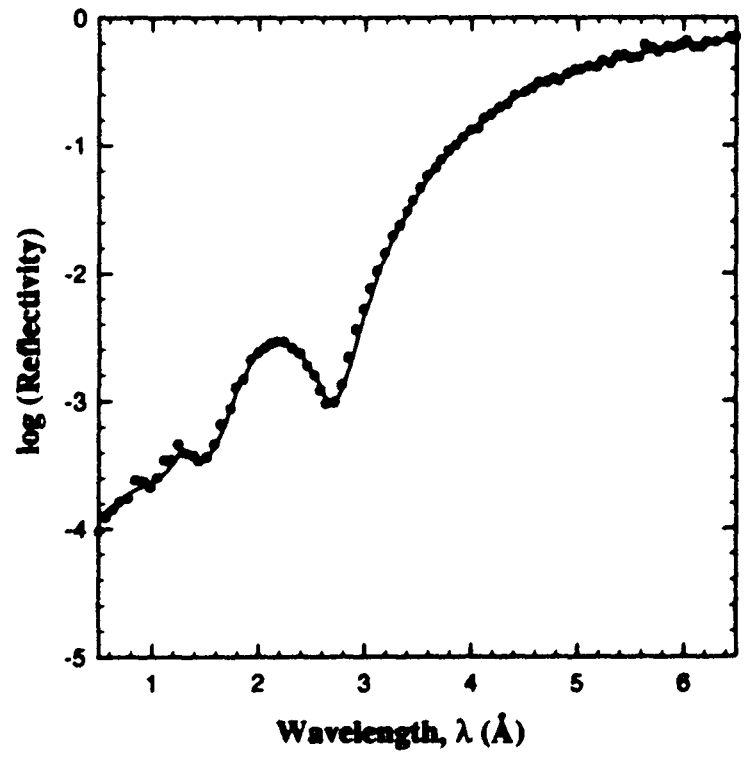

Figure 11: The reflectivity as a function of neutron wavelength for a 800 nm thick PS layer on Si capped with a 20 nm thick dPMMA layer [74]. The sample data (solid circles) are shown with the simulated fit using an interfacial roughness, σ, of 2 nm.

Fitting the interfacial profile using a hyperbolic tangent function for this system an interfacial width of $w = 5.0 \pm 0.5$ nm, was measured after annealing at 170C, confirming the earlier findings of Fernandez *et al* [74]. These findings are notable since the molecular weights and annealing temperatures used in both these systems were markedly different. The theoretical value of interfacial width, w_∞, between homopolymers of infinite molecular weight is given by [76]:

$$2w_\infty = l_\infty = \frac{2a'}{(6\chi)^{1/2}} \qquad (24)$$

where a' is an average statistical segment length of two polymers, and χ is the Flory-Huggins interaction parameter. Using a value of $\chi = 0.04$ and $a' = 0.71$ nm Shull *et al* [77] calculated $w_\infty = 2.9$ nm, which is significantly less than the value obtained by NR measurements [16, 74]. The discrepancy can be accounted for by consideration of contributions associated with fluctuations in the perpendicular position of the interface. These fluctuations are shown schematically in Figure 12. The measured interfacial width, w, is a convolution of the true interfacial width, w_t, and a secondary width, w_0 such that:

$$w = \left(w_0^2 + w_t^2\right)^{1/2} \qquad (25)$$

By inclusion of an appropriate value of w_0, the value of w_t obtained from the measured value of w agrees well with the expected theoretical value [77]. It must be noted that the theoretical width is determined using experimentally derived parameters, notably χ and a, and perhaps some of the discrepancy comes from errors in evaluating these theoretical values.

Studies of the highly immiscible pair of PS and poly(bromostyrene) (PBrS) have been made by Zhao *et al* [26]. The degree of bromination of the PBrS was varied between 84 and 97% a regime which ensures that the PS-PBrS polymers are highly immiscible. Below this degree of bromination the miscibility can be controlled with Br content. A systematic study of the change of the interfacial width with degree of bromination has been performed by Guckenbiehl *et al* [78]. For the highly brominated incompatible PS-PBrS polymer pair and using a deuterated PS Zhao *et al* found that the interfacial width, w, was 4.1 ± 0.5 nm in agreement with X-ray reflectivity measurements. The XR measurements are possible in this case due to the natural contrast provided by the high Br content. There was also a slight variation observed in the interfacial width with molecular weight. Again comparison of the dPS-PBrS interfacial width with theoretical predictions of Helfand and Sapse [76] show that $w_\infty = 1.6$ nm is significantly smaller than the measured width. This cannot be accounted for by correcting for finite chain sizes [79] and as seen before [77] invoking a thermally excited statistical roughness convoluted with the theoretical width (Equation 25) gives a good comparison with the measured width [26].

The temperature dependence of the interfacial width has been investigated using the immiscible polymers of dPS and poly(*n*-butyl methacrylate) (P*n*BMA) [80]. Reflectivity profiles of bilayers of these polymers were obtained as a function of annealing temperature. The interfacial profile was fitted assuming the hyperbolic tangent concentration profile, $\phi(z)$, according to the relationship [73]:

$$\phi\ (z) = \frac{1}{2}\left[1 + \tanh\left(\frac{z}{l_t}\right)\right] \qquad (26)$$

The measured interfacial width, l, is found to vary from 3.2 nm at 393K to 4.3 nm at 429K. Here it was assumed that the intrinsic width l_0 for this system is given by a constant value equal to 1.2 nm. Determination of l_t follows directly by substitution of the appropriate values of l and l_0 in Equation 25.

The interfacial width is directly related to the Flory-Huggins χ interaction parameter. The interface between incompatible polymers is described by minimisation of the free energy function, F, given by [81]:

Figure 12: Schematic representation of the interface between two polymers. The true interfacial width, l_t, (solid line) together with longer range thermal fluctuations, l_o, (dashed line) combine to give a measured interfacial width, l, which is the quadrature sum of these two amplitudes as defined by Equation 25.

$$F = \int_{-\infty}^{\infty} \frac{\phi}{N_1}\ln\phi + \frac{1-\phi}{N_2}\ln(1-\phi) + \chi\phi\,(1-\phi) + \frac{a^2}{24\phi\,(1-\phi)}\left(\frac{\partial\phi}{\partial z}\right)^2 dz \qquad (27)$$

For the case of infinite molecular weight, $N_i \rightarrow \infty$ the hyperbolic tangent function profile described by Equation 26 is an exact solution of Equation 27 and leads to the condition $w_t = w_-$. When the degrees of polymerisation, N_i, of the polymers are finite, then the form of w_t which minimises the free energy of Equation 27 is given by [80, 82]:

$$w_t = 2l_t = \frac{2a}{\sqrt{6}}\left(\chi - \frac{\pi^2}{6}\left(N_1^{-1} + N_2^{-1}\right)\right)^{-1/2} \qquad (28)$$

The values of l_t obtained by Schubert et al [80] allowed χ as a function of temperature to be evaluated using NR and can be shown to follow the relationship $\chi = A + B/\mathrm{T}$, where A and B are constants. Due to the disparity in the value of a for dPS and P*n*BMA of 0.64 and 0.84 nm this leads to values of A equal to -0.0357 and -0.0626 and B of 17.7 and 30.5 respectively for the two extreme values of a. Choosing l_0 to be constant even as a function of temperature may be a little simplistic. It is generally believed that l_0 represents thermally excited capillary waves, and as such must be temperature dependent [26, 77, 83]. However the exact functional form of these capillary fluctuations are at present unsatisfactory for describing all general systems [83, 84]. The value of l_0 chosen by Schubert *et al* however does lead to results that are entirely consistent with their small angle neutron scattering (SANS) results [80].

Many industrially important polymers are either crystalline or semi-crystalline. At temperatures well below the crystalline melt temperature, T_m, the crystallinity causes the surface of films of such polymers to be molecularly rough. This presents problems in the investigation of such interfaces, because thin polymer films on such layers become as rough as the crystalline polymer surface. Traditional neutron reflectivity measurements of such polymer thin film systems at room temperature ($T \ll T_m$) therefore suffer from drastic loss of specular reflectivity associated with this surface roughness. At best the measurements are extremely difficult, but in most cases are more likely to lead to reflectivity profiles which are uninterpretable. Merely heating a thin crystalline polymer film, of for example polyethylene (PE) supported on a polished Si substrate, into the melt regime ($T > T_m$) is insufficient to produce meaningful reflectivity profiles [85]. This failure derives from the remnant long range waviness which remains even after the local molecular roughness is removed. One solution to overcome these problems is use of a sample cell [84] based on the design of solid-liquid cells which are routinely used in neutron reflectivity measurements [86]. The cell consists of a brass trough into which a thick layer of one of the

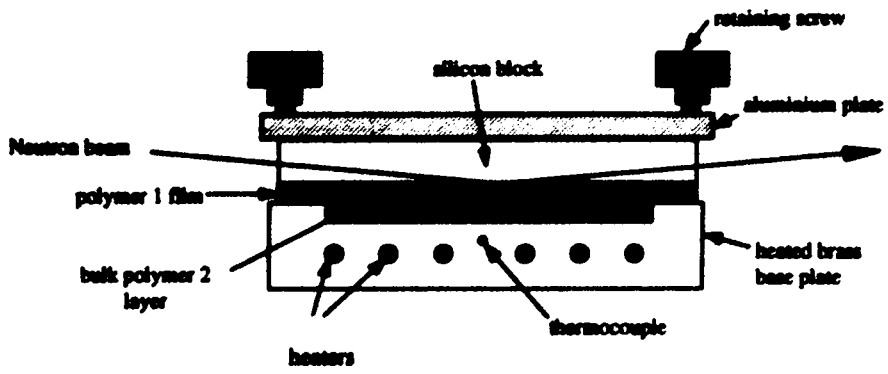

Figure 13: Schematic diagram of the heated cell used to measure NR reflectivity profiles from polymers in the melt

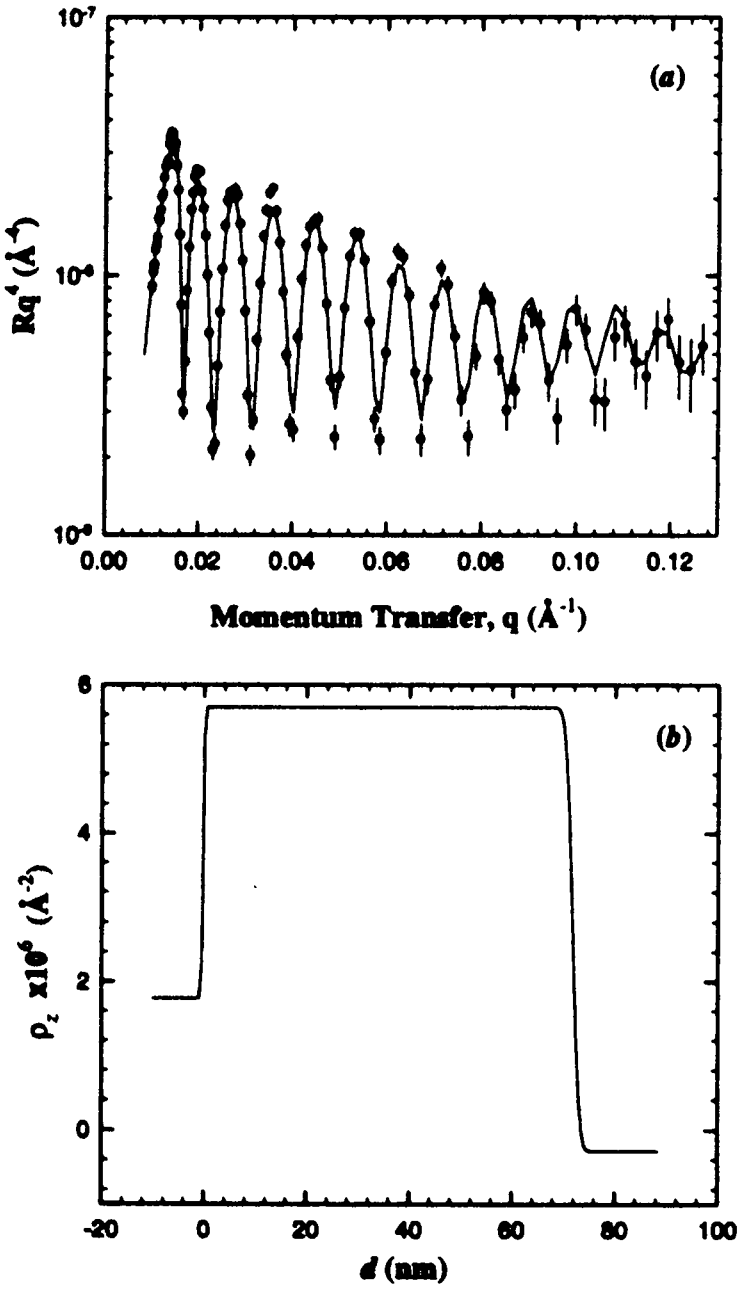

Figure 14: (*a*)Rq^4 versus q reflectivity plot of the dPS - PE system described in the text measured at 150C. The data (solid circles) are over-plotted with the best fit using the model described by the scattering length density profile shown in (*b*) [84].

polymers is held. On top a Si block is placed after coating with the secondary and/or tertiary polymers and held in place with a retaining plate (see Figure 13). The cell is heated via heating cartridges in the brass base and the whole cell held within an inert gas atmosphere to prevent any polymer degradation during the measurements. Si is essentially transparent to neutrons with a transmission efficiency of approximately 90%, enabling the neutrons to pass through the Si to the polymer layers beneath. This method of measuring the interfacial width between polymer pairs is a potentially very powerful technique for determining the χ parameter.

NR measurements using such a cell were used to study the melt interface between d-PS and PE [84]. In these experiments the PE constituted the bulk base layer with a 70 nm thick dPS film spin cast from a toluene solution directly onto the Si. Using this approach reflectivity profiles of the d-PS / PE system were measured at a temperature of 150C, well above the melt temperature of PE and significantly greater than the glass transition temperature of PS. The data collected from this cell are shown in Figure 14(*a*). The lack of damping of the interference fringes even at high q values shows that by including the molecularly smooth and flat silicon surface to which the polymers are moulded, both molecular roughness and long range waviness are successfully removed in the melt regime. Bilayer fits to the data using the model described in Figure 14(*b*) are shown in Figure 14(*a*) as the solid line on the data. The interfacial shape between the dPS and PE is adequately described by a simple Debye-Waller Gaussian roughness. However, the interface width is small enough that differences between a Gaussian and the theoretically predicted hyperbolic tangent gradient (Equation 26) are not distinguishable from these data. The measured interfacial roughness, σ, between these polymers of 1.18 ± 0.33 nm gives w = 2.96 ± 0.84 nm. The theoretical prediction for this interfacial width by Helfand and Sapse at 140C is 1.5nm [76] which again indicates that the measured value of the interfacial width is a convolution of the true (w_t) and intrinsic (w_0) interfacial widths. Hermes *et al* [84] have used various forms of w_0 to try and evaluate w_t from the measured values of w. Following the method of Schubert *et al* [80] a constant value intrinsic width can only be estimated by comparison to other systems since

at room temperature the interface between the dPS and PE is not measurable for the reasons given above. Using Equations 25 and 28 the Flory-Huggins parameter, χ, in the range 0.0116-0.043 are obtained. An alternative approach for determining w_0 is by considering the effect of thermally excited statistical fluctuations (capillary waves) as a χ dependent parameter defined by: [26, 77]

$$w_0^2 = \left(a\rho_0(\chi/6)^{0.5}\right)^{-1} \ln(\lambda_{min}/\lambda_{max}) \quad (29)$$

Where ρ_0 is the segment density and λ_{min} and λ_{max} are the minimum and maximum wavelengths of the capillary fluctuations. Defining w_0 for the d-PS / PE system, using Equation 29 gives a χ value of the order 0.141 at 150C. The apparent discrepancy between the values of χ derived from the different values of w_0 is clearly evident. Recently Xiao *et al* [87] have shown that w_0 between two polymer films is dependent on the film thickness of the top film:

$$w_0^2 = \frac{k_B T}{4\pi\sigma_0} \ln\left(\frac{16\pi^3\sigma_0 d^4}{(w_t^2/2\pi)A}\right) \quad (30)$$

where σ_0 is the interfacial tension, d is the layer thickness, and A is the effective Hamaker constant. This approach has been found to accurately describe the apparent discrepancy between the 'theoretical' and measured width of the dPS-PMMA interface. More recently it has been applied successfully to the dPS-PE and also dPP-PE systems [88].

7.2 Polymer-Polymer Interdiffusion

Interdiffusion of miscible or partially miscible polymers across an initially sharp interface is an area of considerable theoretical as well as practical relevance. This is the model for mixing and welding operations. In practical systems relatively slow polymer molecular relaxation processes can result in interfaces which are metastable or non-equilibrium. As a consequence in these cases it is not enough just to know the morphology and concentration profiles of the resulting interfaces, but also to be able to understand the dynamics of the interdiffusion processes. Interdiffusion over long distances is described by classical (Fickian) diffusion laws, however, polymer chain entanglements make a description of the short-range behaviour complex. Polymers move by reptation, that is motion within and along a tube defined by entanglements of other polymer molecules [89-91]. The observation of the dynamics of the interdiffusion processes is ideally suited to investigation by NR, where it is possible to resolve the early stages where only chain segments move across the initially sharp interface [78, 80, 92-103].

By varying the degree of bromination, x, of the incompatible polymer pair of PS and PBr_xS, the equilibrium interfacial width caused by interdiffusion is seen to depend strongly on x [78]. This is in contrast to the highly immiscible PS-PBrS system described above, where the very high degree of bromination leads to sharp interfaces. Theory predicts that for these partially miscible polymers, intermixing across the interface will continue only until a characteristic interfacial width is reached. For the equilibrium situation the mean-field theory predicts this characteristic width to be [104]:

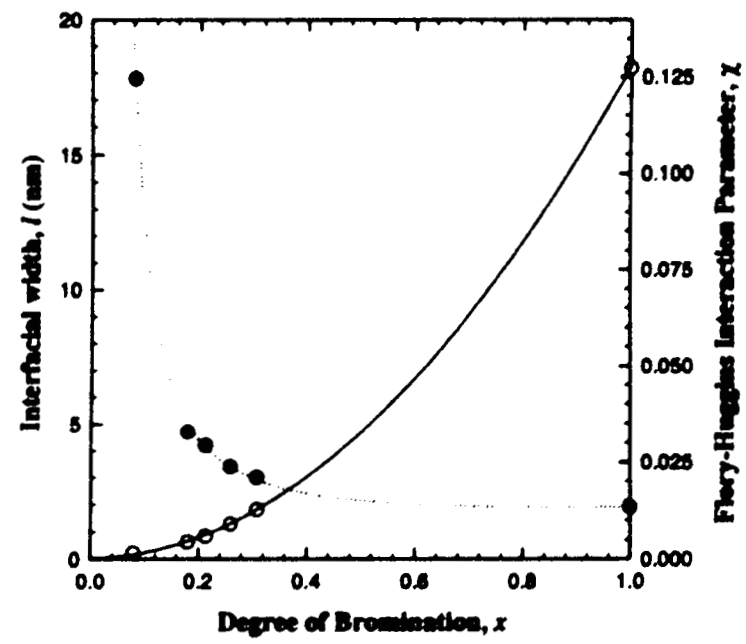

Figure 15: Equilibrium interface width, l, (solid circles), and Flory-Huggins interaction parameter, χ, (open circles) as a function of degree of bromination x for the system dPS/PBr_xS. (Data taken from Ref. [105])

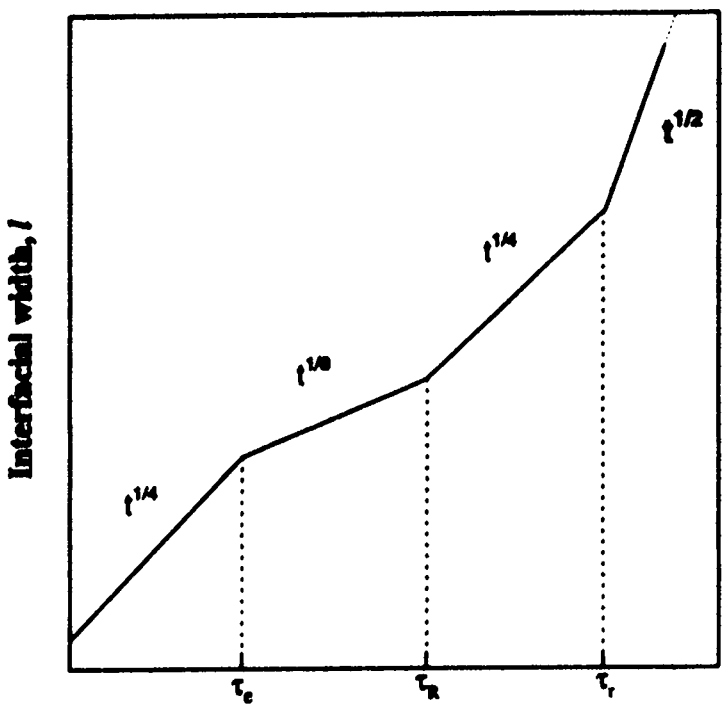

Figure 16: Schematic plot of the interfacial width time behaviour, showing the four time dependencies, characterised by τ_e, τ_R and τ_r as described in the text.

$$w_c = \frac{a\sqrt{2}}{3\sqrt{\chi_c}}\left(\frac{\chi}{\chi_c} - 1\right)^{1/2} \qquad (31)$$

Where χ_c is the critical interaction parameter defined by $\chi_c = 2/N$, N is the degree of polymerisation and other symbols are defined in the text above. The kinetics of the interdiffusion, and also the equilibrium interfacial width of dPS-PBrS bilayers have been studied as a function of degree of bromination, x [105]. The interfacial width was determined from the reflectivity data using a hyperbolic tangent function as predicted by theory [73] for incompatible polymers. The observed time dependence of interdiffusion before reaching equilibrium was shown to follow a growth law with exponent ~0.23 in close agreement to the expected value of 0.25 [106]. The equilibrium interfacial width has a hyperbolic tangent profile and is strongly dependent on the degree of bromination. Indeed if x is reduced below ~0.08 the polymers become completely miscible and interdiffusion will continue until a homogeneous single layer is formed. The interfacial width as function of x is shown in Figure 15, together with values of χ obtained from Equation 31 [105].

The study of interdiffusion between like polymers is possible by use of the isotopic contrast between hydrogenous and deuterated polymers. The resolution of the interfacial profile by NR makes possible the study of diffusion at short annealing times. Of particular interest has been the time dependence of interdiffusion below the reptation time, τ_r. This represents the time required for a polymer chain to move its entire length along the tube produced by the surrounding chains. In practice, at τ_r the interdiffusion process is seen to become Fickian so that $w \propto t^{1/2}$ (see Figure 16). However, in this regime the interfacial width is typically of the order of 20 nm and greater, where NR becomes insensitive and other techniques are required, such as nuclear reaction analysis (NRA) [67] or dynamic secondary ion mass spectrometry (DSIMS) [107, 108] Between τ_r and the Rouse time, τ_R, movement of the chain segments are correlated and $w \propto t^{1/4}$. At $\tau_e \leq t \leq \tau_R$, where τ_e is the entanglement time, movement is restricted by entanglements and gives a $t^{1/8}$ dependence. Below τ_e the segments of the chain no longer experience entanglements and a $t^{1/4}$ dependence is observed.

The effect of molecular weight, M_w, on interdiffusion between h and d-PS has been studied [93]. Lower molecular weight polymer bilayers (Mw = 23300) annealed at 135C for up to 53 minutes produced an interfacial width of 20 nm. The NR profiles were analysed using an error function profile defined by:

$$\phi(z,t) = 0.5\left(1 - erf\left(\frac{z}{2\sqrt{Dt}}\right)\right) \qquad (32)$$

where D is the diffusion coefficient. However, this interfacial profile is Fickian and may not be applicable to short annealing time profiles. Using $M_w \approx 10^6$ the NR profiles of the h/d-PS bilayers could not be fitted using an error function described by Equation 32. Indeed fits were only possible using a more complex reptation model of an error function convoluted with a sharper discontinuous gradient as suggested by theory (see Figure 17). The discrepancy derives from polymer chain fluctuation effects seen for low M_w polymers,

which smears the expected sharp interface into something much more closely representing a broader single error function.

The complex interfacial profile of polymers annealed for short times has been confirmed by the NR measurements of Reiter and Steiner [95] also using very high molecular weight h/d-PS bilayers. They suggested the form of the refractive index profile, n(z), (where n is defined in Equations 1 and 2) to be a superposition of Rouse type motion described by a single continuous function together with a discontinuous profile corresponding to reptation of molecules over distances larger than their tube diameter (see Figure 18):

$$n(z) = \Delta n \left[(1-p)\left(2 - erfc\left(\frac{z}{\sigma_c} \right) \right) + p\left(2 - erfc\left(\frac{z}{\sigma_t} \right) \right) \right] \quad (33)$$

where Δn is the difference in refractive index between h and d-PS, σ_c and σ_t are characteristic interfacial width parameters and p determines the percentage contribution of each of the error functions. For annealing times greater than the Rouse time, τ_R, a $t^{1/4}$ dependence with interfacial width is observed as predicted by theory. At the reptation time, τ_r, the time dependence became Fickian and followed the $t^{1/2}$ dependence expected. For this latter process it is necessary to follow the interface using other techniques such as NRA or DSIMS since the interfacial width becomes too large for the resolution of NR.

The early time interface profiles have also been observed for h- and d-PMMA interdiffusion [103]. Once again a complex interfacial profile is invoked in order to fit the NR satisfactorily. The interfacial widths obtained from the NR profiles show three different time regimes. The first jump in interfacial width corresponding to the initial annealing, followed by an almost constant interfacial width. At $t \sim \tau_R$ the interfacial width increases with time with an approximate $t^{0.3}$ behaviour. These three phases of diffusion mimic quite closely the theoretical predictions shown in Figure 16.

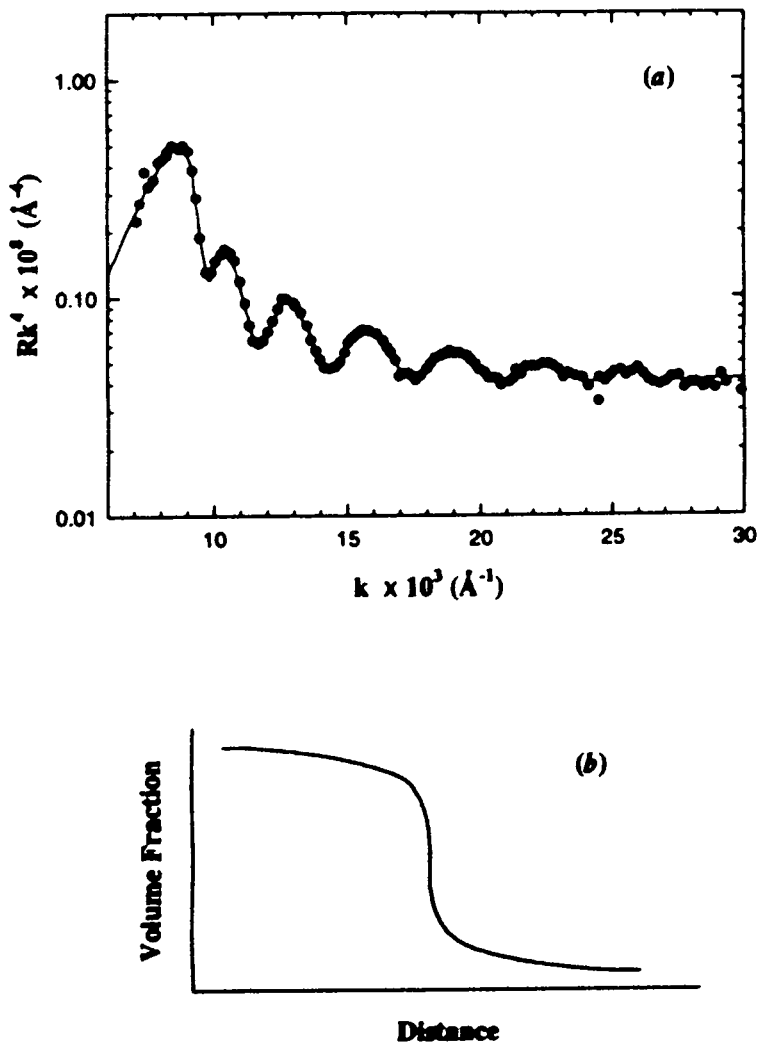

Figure 17: Reflectivity Rk^4 versus k for a bilayered sample of h and d-PS after annealing at 15 minutes for at 155C. The open circles are the experimental data and the solid line is a fit assuming an interfacial profile shape shown in inset. (After Ref. [93])

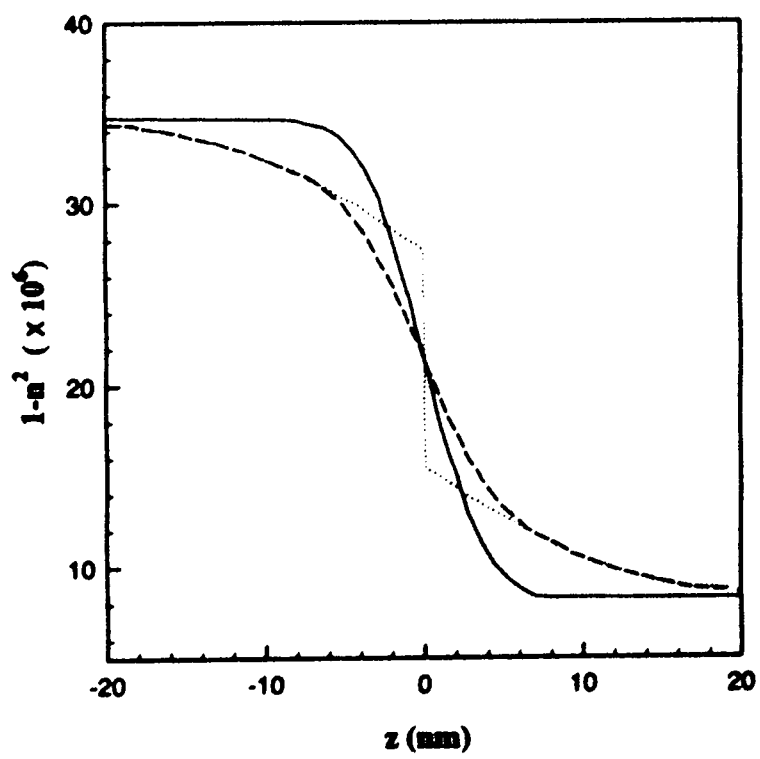

Figure 18: Refractive index profile (solid line) used to analyse the reflectivity data high molecular weight h/d-PS bilayers after short annealing processes, following Equation 33. The two different contributions of the interfacial profile are shown as the dashed and dotted lines (After Ref [95]).

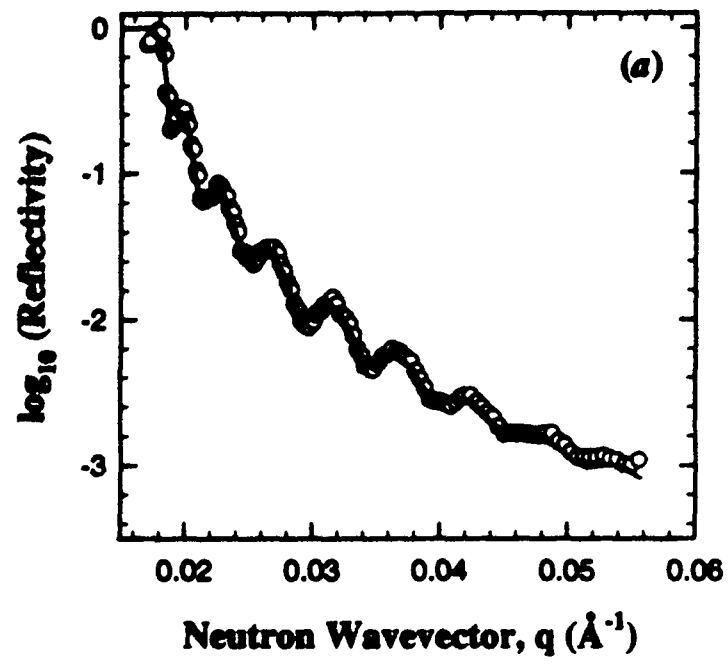

Figure 19: Reflectivity profile of a dPMMA layer on SCPE. The solid line represents the fit assuming the interfacial profile described in (*b*). The interface consists of a linear region on the dPMMA side and a Gaussian tail stretching into the SCPE bulk.

So far only interdiffusion between polymers of similar molecular weight have been discussed. If the molecular weights are very different then as may be expected this has a great effect on the processes of interdiffusion. Fernandez *et al* [97-99, 109] studied the partially miscible polymers of dPMMA and solution chlorinated polyethylene (SCPE), where the molecular weight of the dPMMA was 5 times less than that of the SCPE. Best fits to the data are obtained when using a scattering length density profile of a discontinuity on the dPMMA side of the interface was coupled with a diffuse tail on the SCPE side, see Figure 19. The fits to the data show that after an initial broadening, the width of the interface remains constant with annealing time, but its position is seen to shift towards the dPMMA side. This also corresponds to an increase in the SCPE scattering length density consistent with the idea of dPMMA diffusing into it. Further annealing shows that the interfacial shift towards the dPMMA is much slower. Three time regimes in interfacial broadening are clearly observed, see Figure 20. The behaviour of the polymers are dominated by the differences in their mobility. In general, the more mobile dPMMA swells the less mobile SCPE causing the interface to shift towards the dPMMA without an apparent large increase in width. The changes in time dependence of the interfacial width are consistent with the τ_r of the two polymers. Brochard *et al* [110] have developed a theory for the shape and evolution of the interface between two polymers of differing mobilities. The theoretical and experimental shapes are extremely close and demonstrate once again the detailed structure which can be obtained by NR.

Although much of the experimental work on interfacial interdiffusion has validated many of the proposed theories, little work has concentrated on the effect of confinement on thin film diffusional processes. The effect of frustrated chain confinements near an initially sharp interface are expected to lead to an extra entropic driving force for polymer chain interdiffusion especially for the early annealing

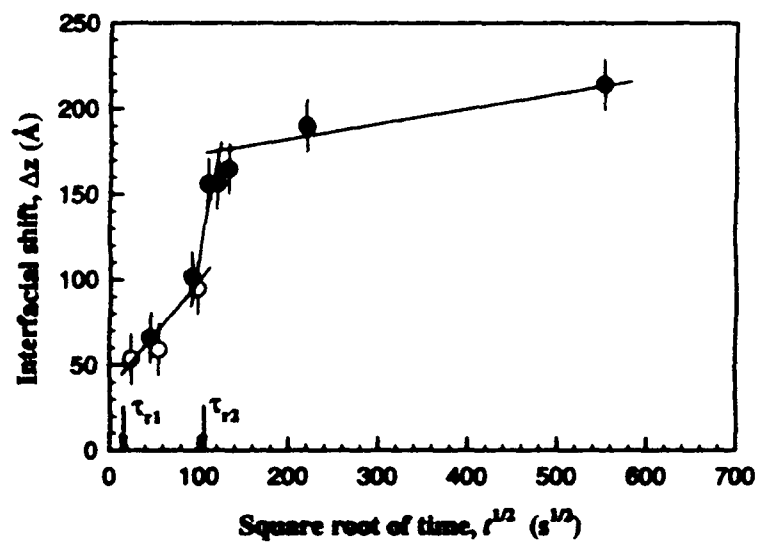

Figure 20: Magnitude of the interfacial shift, Δz, as a function of square root of the annealing time. The reptation times for dPMMA and SCPE are shown as τ_{r1} and τ_{r2} respectively (taken from Ref [99]).

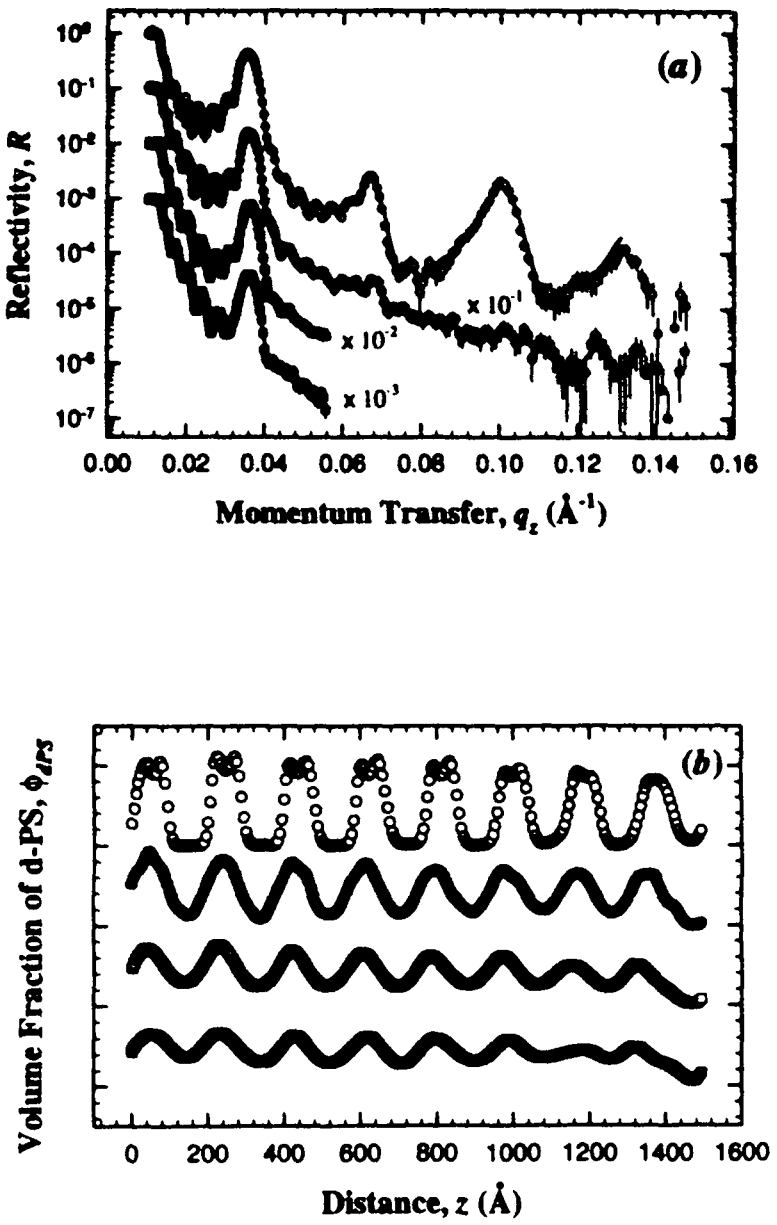

Figure 21: Neutron reflectivity profiles (*a*) and corresponding volume fraction profiles (*b*) obtained from the fits to the data for a multilayer stack of alternating layers d-PS and h-PS. The data represents the sample as made (open circles), after 5 mins annealing at 185 C (closed circles), 55 mins annelaing (open squares) and 135 annealing (closed squares). Plots in both cases have been scaled for clarity (from Ref. [112]).

times [111, 112]. This added driving force is conveniently expressed in terms of a compositional wave vector, ν (= $2\pi/\psi$, where ψ is the wavelength of the compositional fluctuations). In a isotopic multilayer polymer system having an average degree of polymerisation, N, and segment length, a, this gives an enhanced diffusion coefficient [111]:

$$D_E = D\left(1+\frac{Na^2\nu^2}{18}\right)\Lambda(\nu) \qquad (34)$$

where D is the bulk diffusion coefficient and $\Lambda(\nu)$ is the Onsager coefficient. The equation is valid in the regime where the compositional wavelengths, ψ, are of the order of the radius of gyration of the polymer. The benefit of using multilayer stacked layers of isotopic polymers is clear, since this enhanced entropic driving force would be difficult to measure from a single interface between a bilayer sample.

This approach has been applied to multilayer thin film samples of isotopic PS by Jones *et al* [111, 112]. By preparing multilayer samples of alternating hPS and dPS of varying repeat periods, the decay of the composition fluctuations caused by interdiffusion between layers can clearly be seen by the loss of Bragg peak intensity in the NR profiles. By measuring the Bragg peak intensity, for a specific wavevector as a function of annealing time, $I_B(\nu,t)$, the effective diffusion coefficient, D_{eff}, can be obtained [112]:

$$\frac{I_B(\nu,t)}{I_B(\nu,0)} = \exp\left[-\frac{t}{\nu^2 D_{eff}}\right] \qquad (35)$$

Using a sample of repeat period of 18 nm Jones et al [111] observed a diffusion enhancement of a factor of 10, in general agreement with Equation 35. Figure 21 shows a typical NR annealing series for a multilayer sample with fundamental wavelength of 18.7 nm [112]. The higher order Bragg peaks disappear at very short annealing times, within $t \approx \tau_R$, and this is thought to correspond to the entanglement length of PS. Fits to the NR profiles using the MaxEnt approach (see description above) are shown in Figure 21. Ideal Bragg peak intensities are calculated from Fourier transforms of the $\phi(z)$ profiles of Figure 21. Applying Equation 35 gives the values of D_{eff} as shown in Figure 22. Clearly, there is more than one diffusional process occurring as indicated by the change in gradient of $D_{eff}(t)$ plot. This can be further verified by measuring the interfacial width between layers as a function of time. It is seen [112] that the width varies as a power law dependence, such that, $w = t^{\nu}$. For a sample with fundamental wavelength of 18.7 nm annealed

for times much less than τ_r, ν changes from 0.065 to 0.18 for short and long annealing times, respectively. The point of cross-over between these two time regimes is also seen to be dependent on the wavelength, ψ, with slow diffusional behaviour persisting over longer annealing times for smaller wavelengths. These effects are in general agreement with the theoretical contributions to interfacial broadening arising from distribution of chain ends at an interface [73]. Using such multilayer sample geometries these NR results have added further to the understanding of the diffusional processes at short annealing times that would not be easily seen using conventional bilayer samples. Much more work in this area still remains especially with samples of different length scales and using annealing times approaching τ_r.

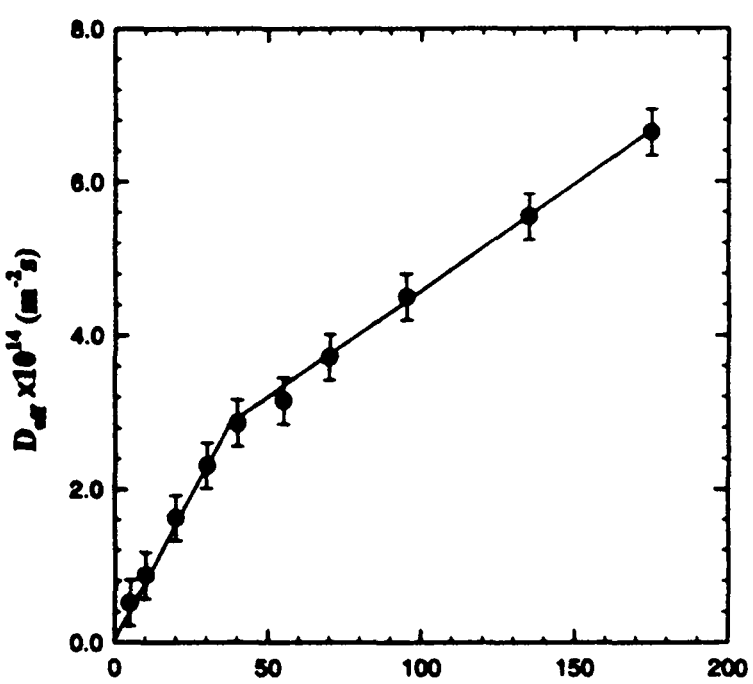

Figure 22: Effective diffusion coefficient, D_{eff}, as a function of time, t, obtained from applying Equation 35 to the data of Figure 21 (from Ref. [112]).

7.3 Segregation Behaviour

It has already been shown that in isotopic blends (a mixture of the deuterated and hydrogenous polymer) the surface composition can be quite different from that of the bulk. Multicomponent polymer systems, in general can produce radically different surface and interfacial properties from those of the bulk and may be dominated by even small amounts of preferentially absorbing species. These segregation properties are of fundamental interest, but perhaps of more practical importance to applications where quantitative control of the surface properties is vital. Surface segregation phenomena are almost universally observed in all multicomponent systems [19-23, 25, 27, 28, 30, 40, 113-128]. The fundamental driving force for these effects is the difference in surface energy. This is controlled by a balance between the gain in surface energy due to segregation and the loss of chemical potential energy as a result of the demixing required to form the surface composition gradient [27, 129-146].

The effect of blending deuterated and hydrogenous polymers has been well studied [19-23, 25-28, 30] as mentioned in Section 5. The effect on symmetric blends, where both polymers have a similar degree of polymerisation, is that the lower surface energy component in this case the deuterated species segregates to the vacuum surface. In contrast, however, to small molecules mixtures of for example fluids or metals, where the effect is confined to a few monolayers below the surface, *ie*, roughly 1 nm, in polymer blends the length scale of decay from the surface to the bulk composition is determined by the size of the polymer molecules, *ie* tens of nanometers. Several depth profiling techniques such as FRES, NRA, DSIMS and NR have been applied to studying these segregation effects. However, although all of the techniques can measure the surface excess of the deuterated component only NR has the resolution to discern the shape of the near surface depth profile with which to test the theoretical predictions.

Mean-field theories for surface segregation [129, 131] predict that the concentration depth profile can be described in terms of the Flory-Huggins free energy of mixing, $G(\phi)$, and the exchange chemical potential, $\Delta\mu$, such that:

$$z = \frac{a}{6}\int_{\phi_s}^{\phi(z)} \left[\phi(1-\phi)\left(G(\phi) - G(\phi_-) - \Delta\mu(\phi - \phi_-)\right)\right]^{-1/2} d\phi \qquad (36)$$

where a is the statistical Kuhn segment length, and ϕ_s and ϕ_- are the surface and bulk volume fractions of the deuterated polymer, respectively. Fits to the reflectivity data for a d/h-PS blend can be described adequately using Equation 36. However as shown in Figure 23, there are small but significant discrepancies between the theoretical prediction and measured data [114].

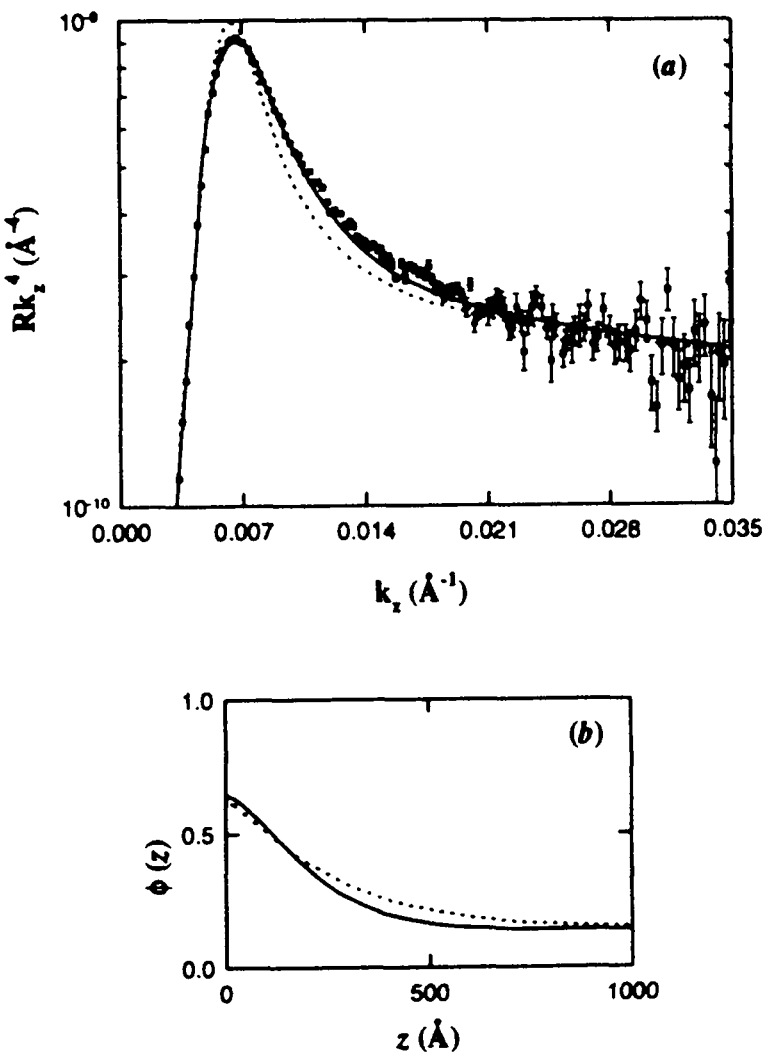

Figure 23: (*a*) Rk^4 as a function of k for a 15% d-PS blend after 7 days annealing at 184C. The dashed line is the best fit to a mean field theory as shown in (*b*). The solid line is best fit assuming the trial function of Equation 37. The difference in the volume fraction profiles are shown in (b) (from Ref [114]).

The reflectivity is very sensitive near the critical edge to the shape of the near-surface dPS concentration profile, due to the increased scattering length density profile causing an effective potential barrier through which neutrons tunnel leading to frustrated total reflection [114]. Better fits to the data in Figure 23 are found when trial functions are used of the form [114, 128]:

$$\phi(z) = (\phi_s - \phi_-)\exp\left(-\left(\frac{z}{\lambda}\right)^{\beta}\right) + \phi_- \qquad (37)$$

where λ is the characteristic decay length and β is a constant. From fits to the data using Equation 37, a decay length of 23.7 nm is obtained [114]. The fact that there are discrepancies between theory and data indicates the power of NR to test theoretical predictions. By making the films thinner the influence of the substrate on segregation effects in addition to the surface can also be studied using NR. Segregation of the dPS to Si substrates is controlled by the presence or absence of the

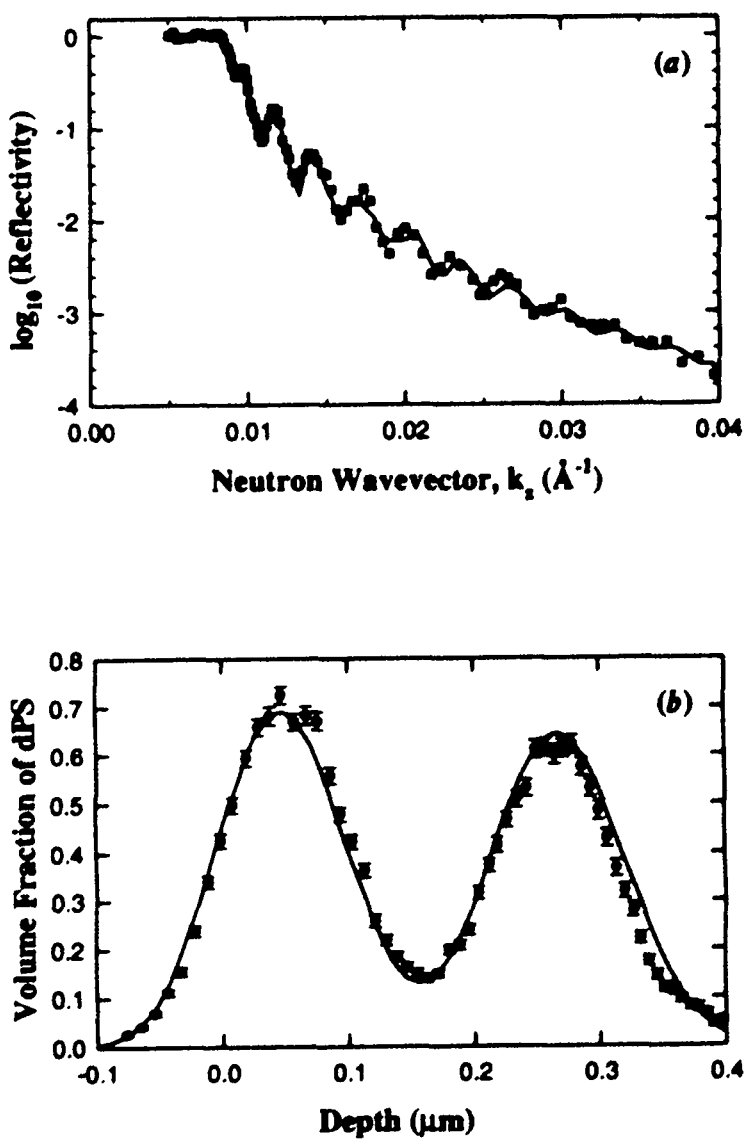

Figure 24: (*a*) Neutron reflectivity data (squares) for a blend of PB and d-PS containing 53.7% by volume of d-PS. The solid line is the fit to the data. (*b*) Volume fraction-depth profile obtained from NRA (circles) over-plotted with the fit to the neutron reflectivity profile after convolution with the resolution of the NRA instrument (from Ref. [122]).

native oxide layer present on Si surface. When the oxide is present segregation of dPS from an isotopic PS blend to both the vacuum and Si substrate interfaces is observed by DSIMS [28]. A greater excess of dPS is observed at the Si substrate than the vacuum surface. By removing the native oxide using a HF etch no segregation to the Si is observed. The mechanism controlling this segregation behaviour is not fully understood at present.

The effect of the presence of a surface on miscible blend phase separation behaviour is dramatic. Spinodal decomposition of blends in such systems no longer follows bulk behaviour where the spinodal composition waves have randomly oriented wave vectors. Instead the surface provides the front from which the composition waves propagate with wave vectors normal to the surface [25]. This surface directed spinodal decomposition effect has been studied most widely using isotopic blends of poly(ethylene-co-propylene) (PEP) [25, 147, 148]. A critical film thickness is apparent below which the early time spinodal wavelength changes to adapt to the film thickness [147]. Surface directed spinodal decomposition has also been observed for blends of miscible or partially miscible polymer pairs [125, 149-151], as well as highly immiscible blends [122, 152], where the spinodal decomposition is triggered by the solvent evaporation in the casting process rather than a temperature quench.

Geoghegan *et al* [122] showed that for a blend of dPS-PB the substrate and vacuum interfaces are rich in dPS. Depth profiling was measured using both NRA and NR. Fits to the NR data convoluted with an instrumental resolution function can be over-plotted onto the NRA data and show a high degree of correlation (see Figure 24). The interfacial profile between the immiscible dPS and PB polymers was fitted using an error function with a characteristic width of 1 nm compared to a theoretical value of 1.3 nm [76, 79] using:

$$l_t = \frac{2a}{\sqrt{6\pi\chi}}\left(1-2\ln\left(\frac{2}{N_1\chi}+\frac{2}{N_2\chi}\right)\right)^{1/2} \qquad (38)$$

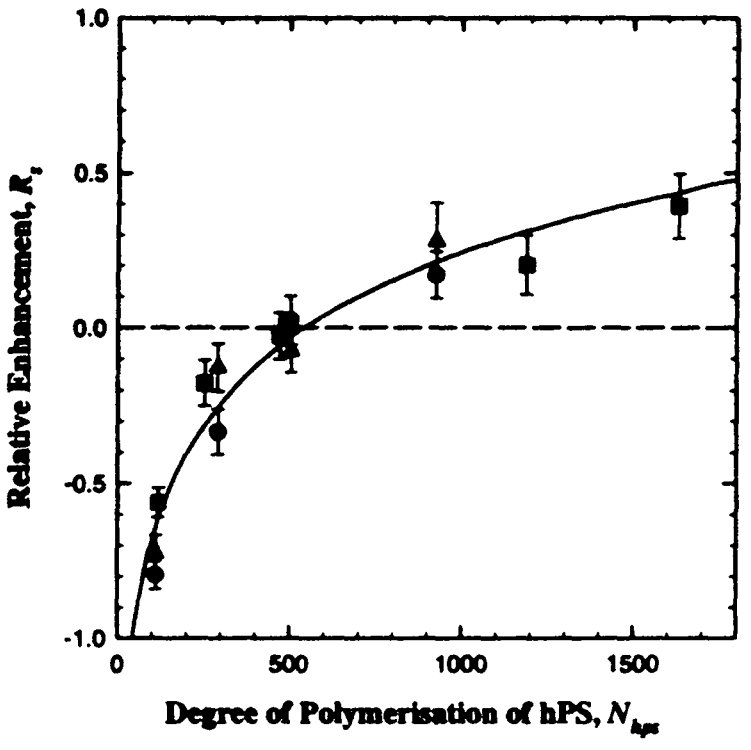

Figure 25: Experimentally determined relative enhancements , $R_s = \phi_s - \phi_\infty / \phi_\infty$, of d-PS at the air-polymer surface as a function of the degree of polymerisation of h-PS (from Ref [27]).

which is the modification of Equation 24 [76] to account for finite molecular weights and polydispersity [79]. Even without inclusion of capillary wave effects the experimental profiles determined by NR are in excellent agreement with theory.

This study was based on an asymmetric polymer pair, where the effects on surface segregation can be dramatic. The surface energy, E_s, is molecular weight dependent such that [122], $E_s = c_1 + c_2 / M_w^{2/3}$, where c_1 and c_2 are constants. For asymmetric polymer pairs the lower molecular weight species will therefore have the lower surface energy and segregate preferentially to the air surface. The effect has been observed for chemically distinct polymer pairs [122] and isotopic PS blends [27]. In the latter study the normalised volume fraction of dPS at the surface obtained from fits to NR profiles, shows both surface excess and depletion as a function of the molecular weight of the hPS (see Figure 25).

The addition of an end group onto a polymer chain is sufficient to drive substantial adsorption of these end functionalised (EF) polymers from a blend of conventionally terminated polymer to both the Si interface [119, 153-156] and/or

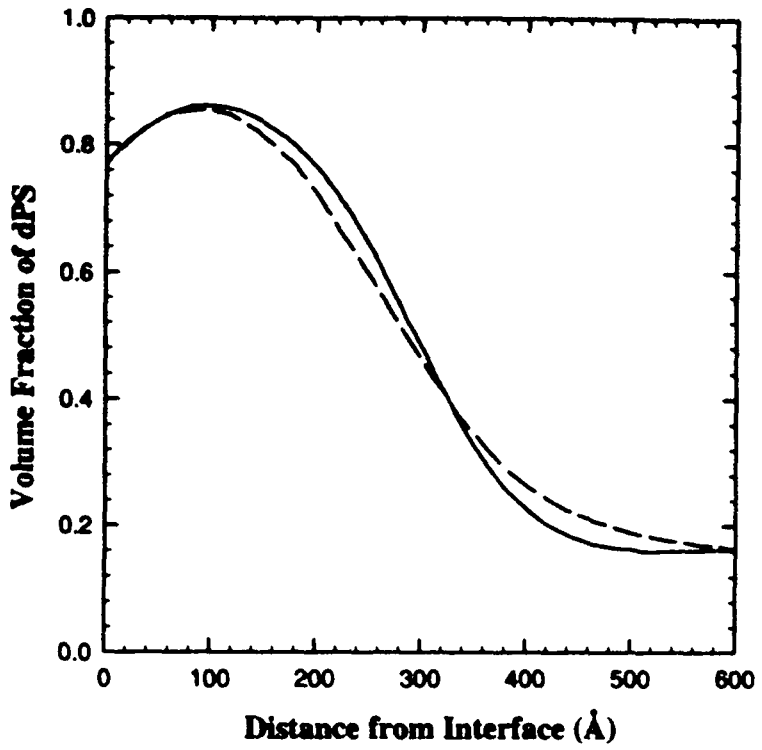

Figure 26: A comparison of the reflectivity measured profile (solid line) for a blend of end-functionalised d-PS and h-PS with the self-consistent field theory for polymer melts, as described in the text (from Ref [153]).

vacuum surface [124, 156]. The functionality of the end group plays the dominant role in this segregation process. In the same manner as isotopic substitution creating segregated layers, the surface excess amounts of these segregated EF polymers create extended layers from the interface. Indeed, the composition profiles of films of purely EF polymers is oscillatory in nature due to the connectivity between end groups and the polymer chain. Since the integrated composition of end groups over the polymer chain length must equal the bulk end group composition then the adsorption layer must be followed by a depletion layer [124]. This behaviour is easily observed by attachment of deutero-styrene monomers adjacent to the EF group. Using such an isotopic substitution scheme for PS, high surface energy carboxylic acid end groups are seen by NR to give a surface depleted in dPS, but enriched at the Si, with the oscillatory composition behaviour resulting from it [124]. If the end group is a low surface energy fluorosilane then the vacuum surface is enriched with this EF group while the Si surface is depleted of them. Again an oscillatory composition behaviour is observed from the fits to the NR data. The oscillatory composition profile is damped, so that the composition of the bulk film is homogenous. The periodicity of the oscillations from the Si substrate are consistent with the R_g of the PS used and independent of end group. However, the periodicity at the vacuum surface is end-group dependent. The fluorosilane terminated PS has a half-layer thickness of 3.9-4.2 nm, and 3.3 nm for the carboxy-terminated PS, compared to the R_g of these polymers of 2.9 nm [124]. The difference can be explained in terms of chain extension and packing. The fact that the end-groups are deuterated does not in this case affect the segregation behaviour since this effect is small in comparison to the influence of the end groups.

When adsorption on a surface from a blend occurs in the melt via an end group, the end tethered chains can be described to have formed a brush. The nature of these brushes is an ideal situation for study using NR. The extent or height of the brush is controlled by the degree of polymerisation of the adsorbing and matrix polymers and the density of adsorbing ends per unit area of interface (the areal density). Two extreme cases of brush are recognised. A 'wet' brush occurs when the matrix polymer molecular weight is considerably less than the adsorbed polymer, and consequently there is a high concentration of matrix polymer in the brush [157]. If however, the matrix chain molecular weight is increased considerably little penetration of the matrix into the brush occurs giving a 'dry' brush. Using a deuterated end functionalised PS (EF-dPS) in a blend of normal PS, the EF-dPS segregates to the Si substrate interface [153]. NR fits to the data are fitted using a functional form for the dPS profile given by [153]:

if $z \geq \lambda_{max}$

$$\phi(z) = \frac{1}{2}\left[(\phi_1 - \phi_\infty) - (\phi_1 - \phi_\infty)erf\left(\frac{z-\lambda_0}{\lambda}\right)\right] \qquad (39)$$

if $z \leq \lambda_{max}$

$$\phi(z) = \phi_\infty - (\phi_\infty - \phi_0)\left(1-\left(\frac{2}{\lambda_{max}}\right)\right)^2$$

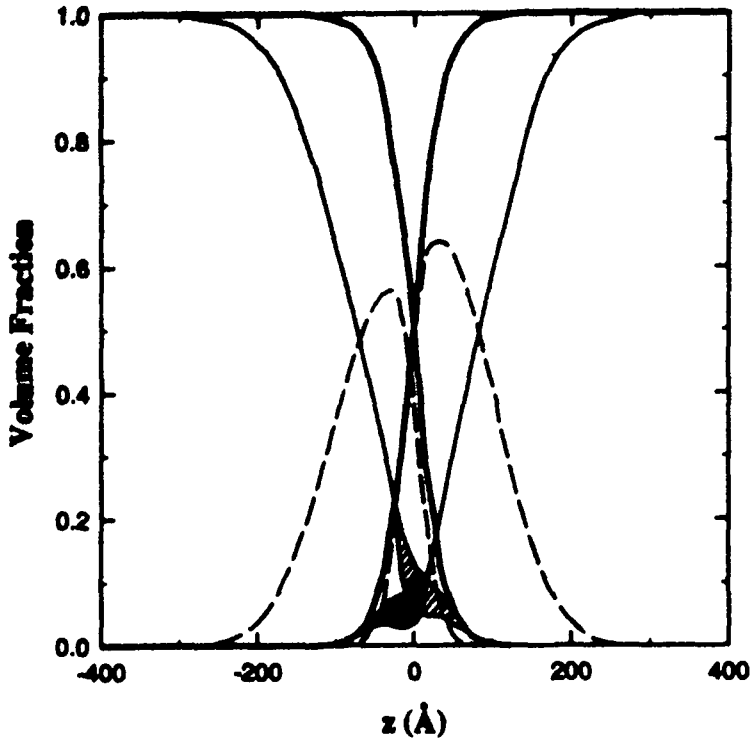

Figure 27: Volume fraction profile of PS and PMMA homopolymers (thin line), the PS and PMMA segments of the copolymer (dashed line) and the total PS and PMMA segments summed over all the homopolymer and respective blocks of the copolymer (thick line). The shaded region is the uncertainty in the homopolymer volume fraction profiles. (From Ref. [175]).

where ϕ_m is the value of ϕ at λ_{max}, ϕ_0 and ϕ_1 are interfacial volume fractions, λ_0 is the error function offset, λ is the error function width and λ_{max} is the position of the maximum. These profiles for the brush shape obtained from fits to the NR data are similar to predictions by self-consistent field (SCF) theories (see Figure 26). The SCF theories take into account both the adsorption energy of the adsorbing chain and also the interfacial interaction parameter [153].

A characteristic feature of the profile is a peak displaced a few nanometers from the surface. No such maximum in the ϕ_{dPS} near surface depth profile is observed for fluoro end-functionalised dPS, where the segregation creates end-tethered chains at the vacuum surface. The driving force is the lower surface energy of the fluorinated end groups. Fits to the NR data used both free-form maximum entropy and also functional form fitting of the form [156]:

$$\phi(z) = \phi_{\infty} + \left(\frac{\phi_s - \phi_{\infty}}{2}\right)\left[1 + \tanh\left(2\left(\frac{z_o - z}{w}\right)\right)\right] \quad (40)$$

where z_o and w are the brush height and width parameters respectively. The brush heights obtained from fits to the NR data are 1.5 times greater than the dry brush predictions of SCF theory, although the variation in surface excess, surface volume fraction and near surface depth profile are consistent between experiment and theory.

7.4 Copolymers At Immiscible Homopolymer Interfaces

Technological interest in polymer blends derives from the potential combination of the properties of individual homopolymers. However, most pairs of polymers form immiscible blends due to the low entropy of mixing of the high molecular weight molecules. The interface between phases of such polymer blends as described above are sharp with only a small extent of interpenetration of molecules. Such interfaces are therefore weak, ultimately leading to a failure in the mechanical properties of the polymer blend due to poor adhesion between phases. It is however, widely known that presence of block or graft copolymers can to some degree alleviate these problems [158-170]. The copolymers segregate to the interface where each block penetrates into its respective homopolymer, forming entanglements with polymer chains from both phases. Due to the covalent bond between the copolymer blocks the effective increase of entanglement density across the interface improves the adhesion. As a result the interfacial tension is reduced [81, 135, 167, 171, 172] leading to a reduction in phase dimension [160, 163, 168, 169, 173]. Therefore knowledge about the distribution of the copolymer at the interface is vital in understanding how copolymers compatibilise immiscible homopolymer blends. NR has shown that with its excellent depth resolution it is an ideal technique for revealing in detail the segment distribution at the interface [109, 170, 174-176]. For diblock copolymers segregated at highly incompatible polymer blend interface, the junction point between the copolymer segments

are expected to be found [135, 172, 177-179] in a thin interfacial layer with extension of the block into the respective bulk phases creating two 'brushes'. As mentioned above, depending on the ratio of copolymer to homopolymer molecular weights two extreme cases of 'wet' and 'dry' brushes could exist.

Using an extensive selective deuteration labelling scheme Russell and co-workers [175] were able to show the distribution of a P(S-b-MMA) copolymers at an interface between PS and PMMA homopolymers, in addition to its individual block segment distributions. The samples were prepared by sandwiching thin layers of copolymer between the PS and PMMA homopolymers and annealing for greater than 5 days at 170 C, before the NR measurements were made. Four different deuterated samples were measured keeping everything else such as layer thicknesses and molecular weights the same. The NR data were fitted assuming the copolymer was segregated only at the interface and has Gaussian interfacial profiles. The interfacial profile of the total PS and PMMA segment distributions were fitted assuming a hyperbolic tangent function as expected from theoretical predictions for the interface without copolymer. By fitting all these four sets of data the composite volume fraction profiles in Figure 27 are obtained.

The exceptional spatial resolution which the distribution of the copolymer and homopolymers are obtained from the NR data is clear. From these data it was seen that the width of the PS-PMMA polymer interface including the copolymer segments is 7.5 nm. This is 25% larger than the interfacial width obtained in the absence of copolymer which was 5.0 nm [16, 74] (see above). This broadening is consistent with the observation that there is seen to be significant overlap of the homopolymers in the interfacial region and is responsible for the reduction in interfacial tension [164].

The area per copolymer chain at the interface can be calculated from the copolymer interfacial distribution [175]:

$$\Sigma = \frac{M_1\rho_1^{-1} + M_2\rho_2^{-1}}{N_A \int_{-\infty}^{\infty} \phi_c dz} \qquad (41)$$

where M_i is the molecular weight of block i with mass density ρ_i and the integral is the integrated copolymer concentration at the interface. For the degrees of polymerisation of copolymer block (N_i) and homopolymer (P_i) in this study it is seen that $N_i = P_i^{3/2}$ and $\Sigma/a^2 < N_i^{1/2}$, where a is the average statistical segment length. This means that the system should conform to the dry brush case [177], which is clearly in contradiction to the observations above which found extensive homopolymer interpenetration.

A study of the influence of the thickness of a P(S-b-MMA) copolymer layer on the interface between PS and PMMA has been performed using NR [176]. The interfacial widths obtained from fits to the NR data assuming a bilayer model and an error function interfacial profile are shown in Figure 28. In the absence of copolymer the width has been measured to be 5.0 nm [16, 74]. As seen previously the

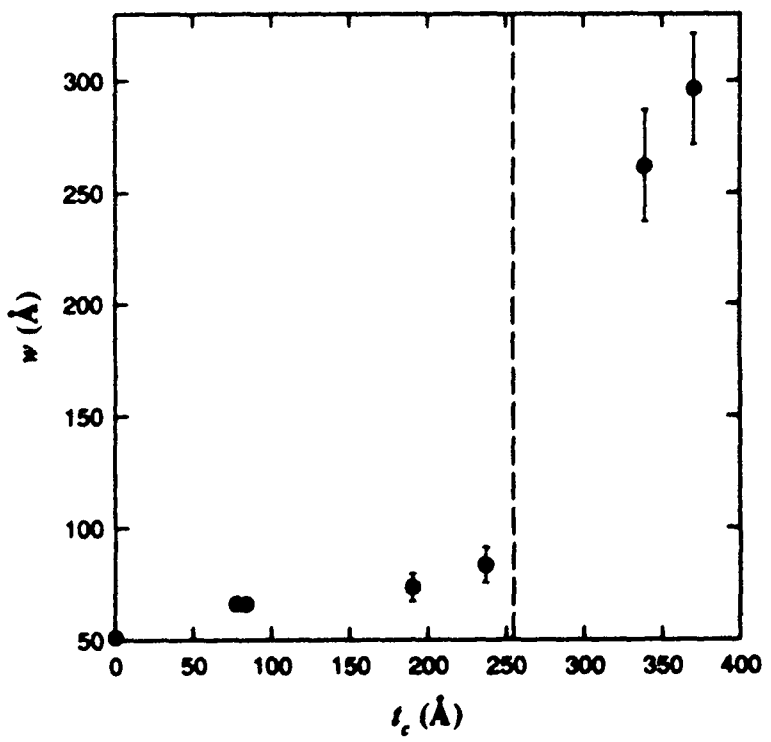

Figure 28: Interfacial width, w, between the PS and dPMMA segments as a function of the thickness of the P(S-b-d-MMA) layer placed between the two homopolymers. The vertical dashed line corresponds to the thickness of the half period of the lamellar microdomain morphology of the diblock copolymer in the bulk (from Ref. [176]).

interfacial width broadens in the presence of copolymer, increasing slightly with increasing thickness of copolymer layer, t_c. However, there is a discontinuity observed in the behaviour at the copolymer layer thickness of ≈ 25 nm, where the apparent interfacial width becomes very large, > 25 nm. At the discontinuity, the thickness, $t_c \approx L/2$, where L is the period of copolymer microdomain lamellar in the bulk. When the copolymer layer thickness exceeds ≈ $L/2$ then the interface becomes saturated with copolymer and additional copolymer microstructures are formed either side of the interface [135, 180, 181] and care must be taken in the interpretation of the results [174, 176, 180]. Using the NR data measured these additional microstructures can not be distinguished from the possible interfacial curvature resulting from the vanishing interfacial tension caused by the copolymer [167, 176].

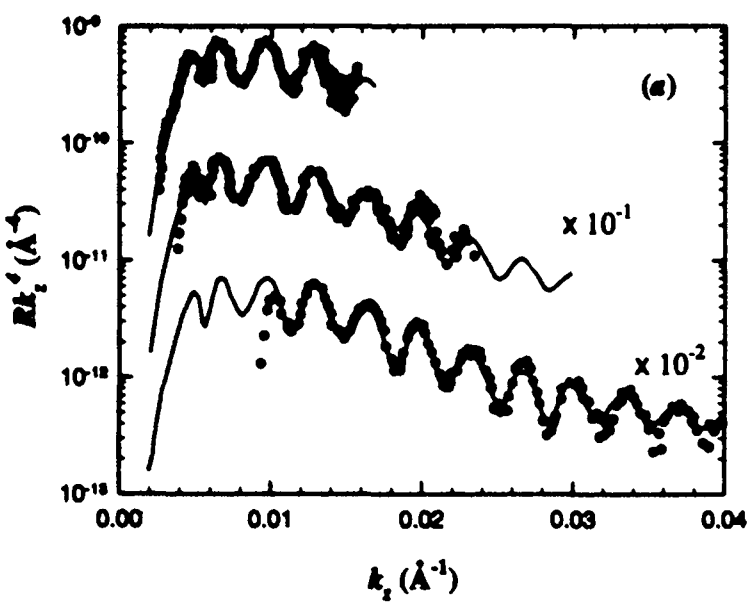

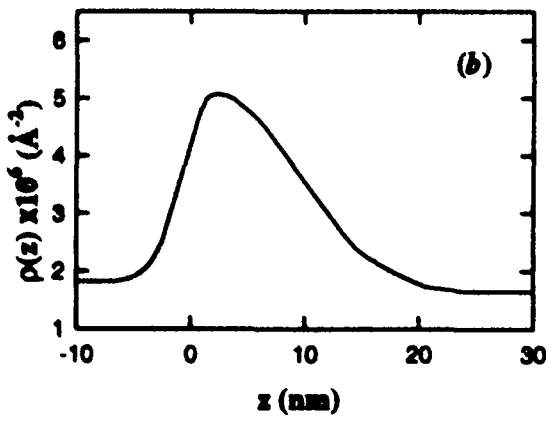

Figure 29: (*a*) Neutron reflectivity profiles of a d-PS-b-PVP diblock copolymer at the PS-PVP homopolymer interface together with the bet fit to the data (solid lines). The best fit is shown as a scattering length density profile shown in (*b*) (from Ref.erence [174]).

By mixing the copolymer with the homopolymers before bringing the homopolymer layers together a more realistic equilibrium picture of copolymer interfacial segregation can be achieved [174, 180, 182]. Using this sample preparation approach a number of studies of the PS and poly(vinyl pyridine) (PVP) and P(S-b-VP) copolymer system has been made using both forward recoil spectroscopy [182] and NR [174]. Dai *et al* [174] showed that from hyperbolic tangent interfacial profiles fits to the NR data the bare PS-PVP homopolymer interface has an interfacial width, w = 3.4 nm. This compares to a theoretical values of 1.66 nm determined using the Broseta modification [79] of the Helfand and Sapse theoretical width [76] (Equation 38). However, the difference can be reconciled by inclusion of capillary waves following as seen above [26, 77] using Equations 25 and 29. At equilibrium the copolymer is found to segregate to the PS-PVP interface [135, 174] and the exact distribution of the deuterated block of the copolymer has been obtained using NR as a function of the bulk volume fraction of copolymer in the homopolymer, ϕ_∞, see Figure 29.

The segregation isotherm, a plot of copolymer interfacial excess, z_i^*, as a function of copolymer volume fraction in the bulk homopolymer, ϕ_∞, is obtained by evaluation of z_i^*, from:

$$z_i^* = \frac{N_c}{N_{dPS}} z_{dPS}^* = \frac{N_c}{N_{dPS}} \int_{-\infty}^{\infty} \left(\phi_{dPS}(z) - \phi_{dPS}(\infty)\right) dz \qquad (42)$$

The segregation isotherm obtained from the evaluation of fits to the NR data using Equation 42 can be adequately described by theory [135, 179]. The interfacial copolymer volume fraction profile shows a slight discrepancy between the self consistent mean field (SCMF) calculations [135] and NR evaluated data, since the SCMF theory predicts slightly sharper interfacial widths. By convolution with a Gaussian resolution function the SCMF prediction falls

exactly on the measured profile. As the amount of interfacial copolymer increases the interfacial tension between the homopolymer phases decreases, such that [182]:

$$\gamma = \gamma_0 - \frac{\rho}{N_c}\int_{-\infty}^{\mu} z_i^* d\mu \qquad (43)$$

where μ is the calculated chemical potential from SCMF theory, γ_0 is the interfacial tension in absence of copolymer, and ρ and N_c are the segment density and degree of polymerisation of the copolymer. From Equation 29 it is seen therefore that as the interfacial tension decreases with increasing amount of copolymer at the interface, this leads to an increase in capillary wave amplitude. These measurements which test the relevant theories are only possible with the excellent resolution that NR provides.

7.5 Diblock Copolymers

The microdomain morphologies of diblock copolymers in the bulk has been studied extensively using both scattering and optical techniques (see for example Reference [183]). In thin film geometry the ordering is strongly influenced by the interactions with the surfaces. An oscillatory concentration depth profile is expected perpendicular to the surface due to the segregation of the chemically distinct but molecularly connected segments of the copolymer [184, 185]. Diblock copolymer ordering has been studied on pure copolymer films on silicon [16, 186-190] or confined between solid walls [191-193] and also in the presence of solvent [194] or homopolymer [195, 196] and reviewed recently in Reference 75. Only with the use of NR measurements has the full detail of such diblock copolymer ordering phenomena in thin films been possible to evaluate experimentally.

In the bulk, symmetric diblock copolymers undergo a weak ordered to disordered phase transition from ordered lamellar morphology to a phase-mixed morphology [197,198] at a temperature T_{ODT}. This occurs when the relationship, $\chi N = 10.5$ is satisfied [199]. However, near an interface the preferential segregation of one of the copolymer blocks to an interface induces an ordering of the phase-mixed copolymer far from T_{ODT} [187, 188]. Since χ is in most cases inversely proportional to temperature, then by heating a sample the copolymer is forced from an ordered to disordered state. By selective deuteration of one of the blocks of the copolymer this temperature dependent ordering of symmetric diblock copolymers of P(S-b-MMA) has been studied using NR measurements by Menelle *et al* [188]. In the fully ordered state the copolymer is seen to form lamellae parallel to the Si surface with a lamellar period of L_0. The PMMA segments segregate preferentially to the Si surface and the PS segments to the air surface. The PMMA layer at the Si surface is only half the thickness of the lamellar repeat period, *ie* $L_0/2$ [16, 87-189, 190]. A typical NR profile obtained from these well ordered films is shown in Figure 30. Several orders of Bragg reflections are observed which indicate that lamellae are formed parallel to the Si and air surfaces. The Bragg peaks have narrow widths indicating that the lamellar layer

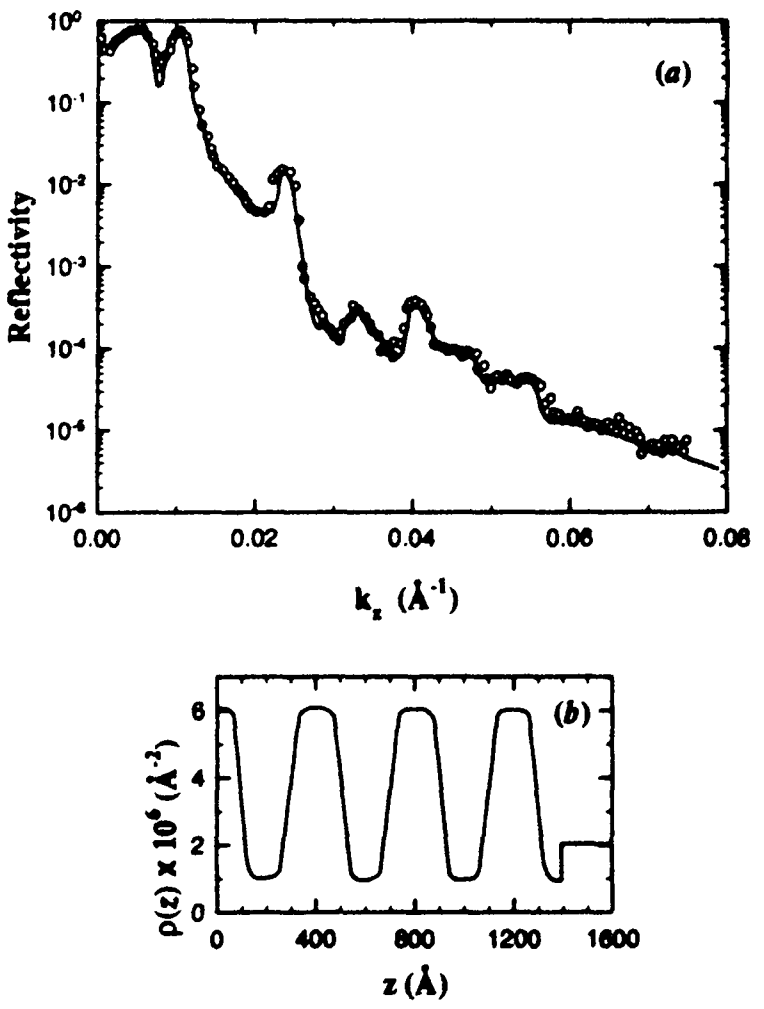

Figure 30: (*a*) Neutron reflectivity profile of an annealed thin film of P(d-S-b-MMA) diblock copolymer. The solid line is the fit to the data shown in (*b*) (from Ref. [16]).

thicknesses are very uniform. The lamellar thickness can be calculated from the position of the first Bragg peak using the Bragg Law [200]:

$$\left(\frac{\pi}{L_0}\right)=\left(\frac{q_{pk}^2-q_c^2}{4}\right)^{1/2} \qquad (44)$$

where q_{pk} and q_c are the positions of the first Bragg peak and the critical edge, respectively. Fits to such NR profiles indicate that indeed the lamellar are very uniform in thickness with interfacial widths between PS and PMMA segments of 5.0nm for all the copolymer molecular weights measured [16].

As seen before this value is slightly larger than the theoretical value of 4.0 nm calculated from SCMF theory [77], but can be accounted for by inclusion of capillary waves (see above). By partial deuteration of small segments of either one end of one copolymer chain or those adjacent to the junction point, a very detailed study of chain configuration in well ordered films is possible using NR [189, 190]. The chain ends are found to be well distributed within the corresponding domains with a weak maximum in distribution occurring at the domain centres. The junction points are strongly segregated to the interfacial region. The volume profiles from results of these NR measurements fit exactly to independent predictions from SCMF theory [77]. If such well ordered films are annealed at increasingly higher temperatures the high order Bragg reflections are gradually lost and the first-order reflection broadens and diminishes [188], which is consistent with a disordering of the lamellae. However, as fits to the NR data show, not all the ordering is lost even when well above T_{ODT} [187, 188] and near the surfaces lamellae still exist. This ordering is damped so that in the bulk of the film a homogeneous scattering length density is observed indicating a disordered copolymer morphology [188]. Fits to the reflectivity data (see Figure 31) can be described using a volume fraction profile for the PS segment as a combination of two exponential decaying oscillatory functions:

$$\phi_{PS}(z)=\max\left[\phi_a e^{-\frac{z}{\xi}}\cos\left[\frac{2\pi z}{\overline{L}}\right],\ \phi_s e^{-\frac{E-z}{\xi}}\cos\left[\frac{2\pi(E-z)}{\overline{L}}\right]\right]+\overline{\phi}_{PS} \qquad (45)$$

where ϕ_a and ϕ_s are the air and silicon excess concentrations of PS, ξ is the decay length of the damping, $\overline{L}$ is the average lamellar period, E is the total copolymer film thickness and $\overline{\phi}_{PS}$ is the average concentration of PS in the copolymer. The fits to reflectivity are extremely sensitive to these parameters. Except for the highly ordered state, L is not constant within the thickness of the film and varies with an empirical form given by:

$$L(z)=\overline{L}+\Delta L\sin\left[2\pi\left(\frac{E-z}{E}\right)\right] \qquad (46)$$

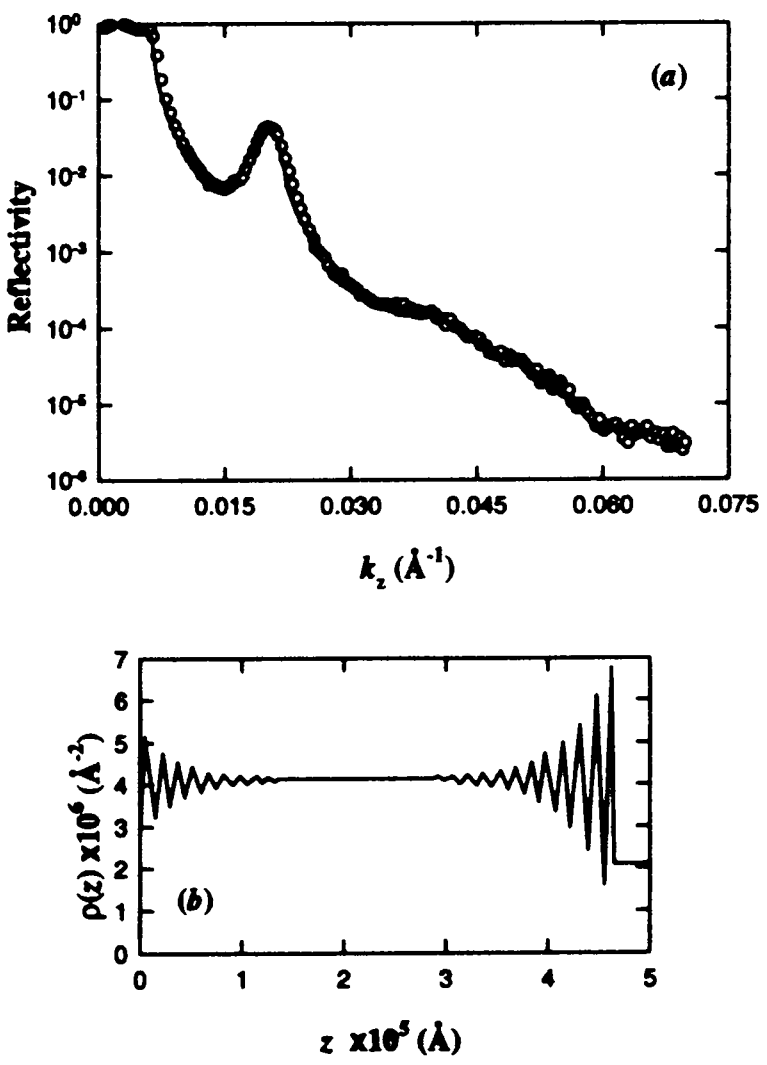

Figure 31: Neutron reflectivity profile (*a*) and scattering length density profile fit to the data (*b*) for a symmetric thin film of a P(d-S-b-MMA) symmetric diblock copolymer annealed at 185C (from Ref. [188]).

where ΔL is found to be ≈ 3.0 nm. In addition, the first-order Bragg peak intensity is very sensitive to the magnitude of ξ. The values of ξ and L obtained from NR agree extremely well with the values predicted from theory [184, 187]. As from Equation 45 for all temperatures there is partial ordering of the copolymer. However, as the temperature decreases $\xi \rightarrow \infty$ at which point the copolymer becomes fully ordered [188]. This transition temperature, T_-, is inversely proportional to film thickness. For these P(S-b-MMA) diblock copolymers as $E \rightarrow \infty$, T_- is seen to asymptote to a value of T = 157.7C which corresponds to the value of T_{ODT} for a bulk copolymer specimen.

So far copolymer films have been described where lamellae formation occurs with each surface adsorbing a different component. These films are called asymmetric films [108]. A symmetric films results when the same block segregates to both surfaces [186]. Incommensuration of the copolymer layers occurs for film thickness, E, and natural lamellar period, L_0, if $E \neq nL_0$ for symmetric films or $E \neq (n+½)L_0$ for a asymmetric films. These effects can be accommodated in films where E is large

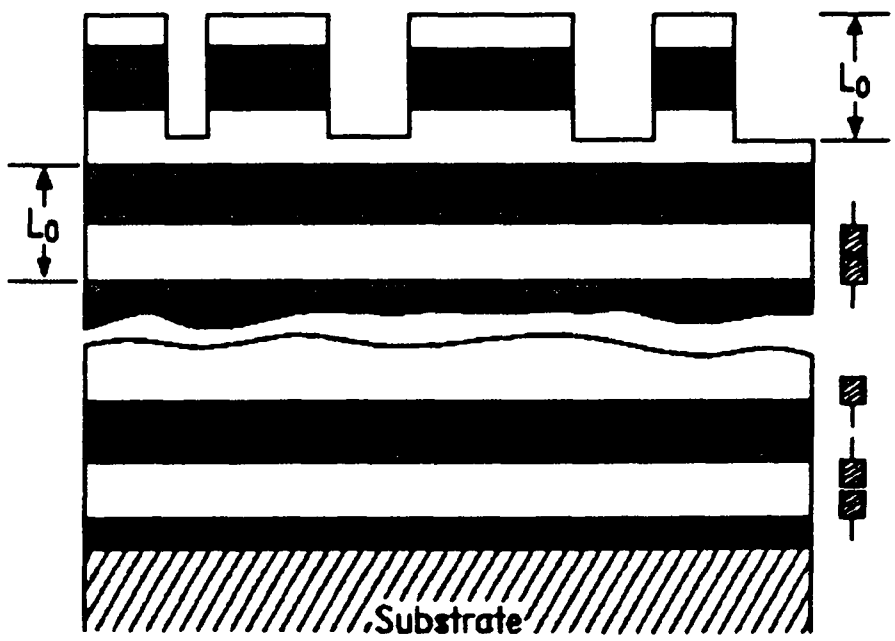

Figure 32: Schematic representation of a diblock copolymer multilayer with preferential segregation of one block to both the substrate and the air interfaces (antisymmetric segregation). The frustration between total thickness and number of lamellae results in step formation at the air surface (from Reference [191]).

since the incommensurate thickness can be distributed among the large numbers of lamellar. However, for the case of asymmetric thin films where $E \neq (n+½)L_0$ the constraint is relieved by formation of islands or holes on the free surface with a height of L_0 (see Figure 32). Fits to NR profiles of such P(S-b-MMA) symmetric diblock copolymer thin films show that the experimentally determined lamellar period, L, also varies about the expected bulk value L_0 as a function of the layer thickness, E [191]. If such a P(S-b-MMA) copolymer film is coated with a thick Si oxide layer (buffered by a very thin high molecular weight PMMA layer to prevent damage to the copolymer during sputtering of the oxide) the copolymer is then confined between two solid walls. In this case the PMMA preferentially adsorbs to the Si surfaces giving a symmetric film. In such films terrace formation is suppressed [192, 193, 201] and development of the period L_0 for parallel multilayer lamellar formation is frustrated.

A perturbed period, *ie* $L \neq L_0$, is formed for thicknesses $E \neq nL_0$. As a function of E, L the measured lamellar thickness determined from NR measurements also oscillates about the value of L_0 as seen for the asymmetric films. Examination of the NR profiles from these symmetric films shows that the third-order Bragg reflection shifts to lower q_z as E/L_0, the reduced film thickness increases [191-193]. As can be seen from Equation 44, this indicates that the copolymer period increases with increasing film thickness. However, further increases in E/L_0 results in a pronounced growth in a shoulder of the third-order Bragg reflection as higher q_z's, which eventually replaces the peak at smaller q_z. A plot of the thickness divided by the measured period (E/L) as a function of the thickness divided by the equilibrium period(E/L_0) is shown in Figure 33. Clearly the number of measured layers, *ie* E/L, is always an integer, whereas the number of periods, *ie* E/L_0, goes through a transition at half integer values of E/L_0. This corresponds to the point of maximum frustration for the lamellar layers and the number of layers abruptly changes by one. This discretely changing step behaviour persists over a large range of thickness, but diminishes with increasing number of layers [75, 193]. Detailed

fits to the reflectivity data reveal that the interdomain widths between the PS and PMMA phases, w, varies as a function of L. When $L/L_0 < 1$ the multilayers are compressed and w is seen to be less than the calculated equilibrium unperturbed value. Conversely, when the layers are expanded ($L/L_0 > 1$) the width is slightly larger than the unperturbed value [75]. These variations in L contradict SCMF theory [185, 202], which predicts a constant value. Russell proposes that the capillary amplitude is suppressed or increased in the compressed or expanded layers, respectively, leading to changes in capillary wave amplitude, w_0, and hence w (see above, Equation 25).

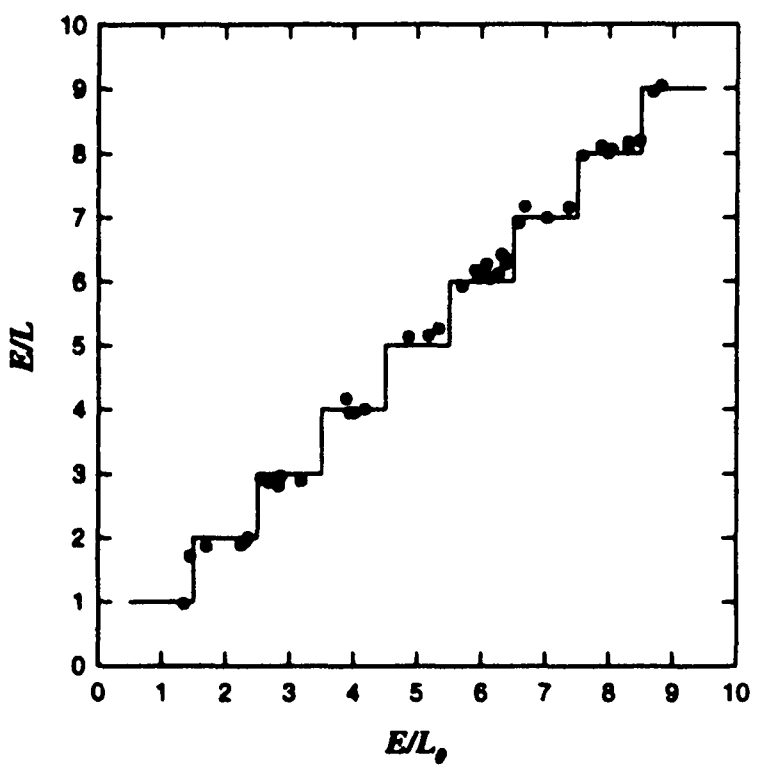

Figure 33: Number of periods confined between two solid surfaces, E/L, for a P(d-S-b-MMA) diblock copolymer, as a function of the reduced film thickness, E/L_0 (from Ref. [75]).

Work is currently focusing on controlling the orientation of the copolymer microstructure. Attempts have been made to produce perpendicular alignment between solid Si confining walls by coating these surfaces with random P(S-r-MMA) copolymers. At the point of maximum frustration a perpendicular orientation is predicted since there is no preferential adsorption [203]. From NR measurements the total loss of the third-order Bragg reflection at a reduced thickness $E/L_0 = 2.52$ together with loss of intensity in the first-order peak indicates some copolymer is ordered in directions other than parallel to the walls. SANS from this sample confirms it is due to the presence of perpendicular copolymer alignment [192].

8. CONCLUSIONS

This article has briefly reviewed the technique of neutron reflectivity together with some highlighted aspects which make it such a powerful tool in the hands of polymer scientists. A review of some areas to which reflectivity has been applied has shown that the technique has made and continues to make significant contributions to the understanding of polymers at surfaces and interfaces. The ability to selectively label sections of molecules or whole molecules in conjunction with the sensitivity of neutron reflectivity has permitted investigations of phenomena which are not possible by any other technique.

ACKNOWLEDGEMENTS

The authors would like to acknowledge the American Chemical Society and Elsevier Science, The Boulevard, Langford Lane, Kidlington, OX 5 1GB,UK and also Sara Burgerhartstraat 25, 1055 KV Amsterdam, The Netherlands for kind permission to reprint figures from the journals that they publish.

REFERENCES

1. Lekner J, *Theory of Reflection*, 1987, Martinus Nijhoff, Dordrecht
2. Higgins JS & Benoit HC, *Polymers and Neutron Scattering*, 1994, Clarendon Press, Oxford
3. Koester L, in Bonse U & Rauch H (eds), *Neutron Interferometry*, 1979, Oxford Science Publications, Oxford
4. Sear VF, *Neutron News*, 1992 **3**, 26
5. Born M & Wolf E, *Principles of Optics*, 1980, Pergamon Press, Oxford, 6th edition
6. Russell TP, *Mater Sci Rep*, 1990, **5**, 171
7. Heavens OS, *Optical Properties of Thin Films*, 1955, Butterworth, London
8. Penfold J, *Physica B*, 1991, **173**, 1

9. Bucknall DG, Penfold J, Webster JRP, *et al*, ICANS XIII Proceedings, *PSI Proc 95-02*, 1995, **1**, 123
10. Stamm M, Hüttenbach S & Reiter G, *Physica B*, 1991, **173**, 11
11. Karim A, Arendt BH, Goyette R, Huang YY, Kleb R & Felcher GP, *Physica B*, 1991, **173**, 17
12. van Well AA, de Haan VO & Fredrikze H, *Physica B*, 1994, **198**, 217
13. Clemens D, *Physica B*, 1996, **221**, 507
14. Sun X, Brouchard E, Lapp A, Farnoux A, Daoud M and Jannick G, *Europhys Letts*, 1988, **6**, 207
15. Sun X, Farnoux B, des Cloizeaux J & Jannick G, *Physica B*, 1989, **156/157**, 407
16. Anastasiadis SH, Russell TP, Satija SK & Majkrzak CF, *J Chem Phys*, 1990, **92**, 5677
17. Vaknin D, Kjaer K, Als-Nielsen J & Lösche M, *Makromol Chem Macromol Symp*, 1991, **46**, 383
18. Lu JR, Hromadova M, Simister EA, Thomas RK & Penfold J, *J Phys Chem*, 1994, **98**, 11519
19. Bates FS, Wignall GD & Koehler WC, *Phys Rev Lett*, 1985, **55**, 2425
20. Bates FS & Wignall GD, *Phys Rev Lett*, 1986, **57**, 1429
21. Pan DH & Prest Jr WM, *J Appl Phys*, 1985, **58**, 15
22. Jones RAL, Kramer EJ, Rafailovich MH, Sokolov J & Schwarz SA, *Phys Rev Lett*, 1989, **62**, 280
23. Jones RAL & Kramer EJ, *Philosophical Mag B*, 1990, **62**, 129
24. Leonhardt DC, Johnson HE & Granick S, *Macromolecules*, 1990, **23**, 685
25. Jones RAL, Norton LJ, Kramer EJ, Bates FS & Wiltzius P, *Phys Rev Lett*, 1991, **66**, 1326 & Jones RAL, *Phys Rev Lett*, 1991, **66**, 1326
26. Zhao W, Zhao X, Rafailovich MH, Sokolov J, Mansfield T, Stien RS, Composto RC, Kramer EJ, Jones RAL, Sansome M & Nelson M, *Physica B*, 1991, **173**, 43
27. Hariharan A, Kumar SK & Russell TP, *J Chem Phys*, 1993, **98**, 4163
28. Hariharan A, Kumar SK, Rafailovich MH, Sokolov J, Zheng X, Duong D, Schwarz SA & Russell TP, *J Chem Phys*, 1993, **99**, 656
29. Graessley WW, Krishnamoorti R, Balsara NP, Fetters LJ, Lohse DJ, Schulz DN & Sissano JA, *Macromolecules*, 1993, **26**, 1137
30. Hong PP, Boerio FJ & Smith SD, *Macromolecules*, 1994, **27**, 596
31. Bartell LS & Roskos RR, *J Chem Phys*, 1966, **44**, 457
32. Sivia DS, Hamilton WA & Smith GS, *Physica B*, 1991, **173**, 121
33. Press WH, Teukolsky SA, Vetterling WT & Flannery, *Numerical Recipes*, 2nd ed, Cambridge University Press, Cambridge, 1992
34. Sinha SK, Sirota EB, Garoff S & Stanley HB, *Phys Rev B*, 1988, **38**, 2297
35. Pynn R, *Phys Rev B*, 1992, **45**, 602
36. Pynn R & Baker S, *Physica B*, 1994, **198**, 1
37. Névot L & Crocé P, *Phys Appl*, 1980, **15**, 761
38. Cowley RA & Ryan TW, *J Phys D*, 1987, **20**, 61
39. Kunz K, Reiter J, Götzelman A, Reiter J & Stamm M, *Macromolecules*, 1993, **26**, 4316
40. Geoghegan M, Jones RAL, Sivia DS, Penfold J & Clough AS, *Phys Rev E*, 1996, **53**, 825
41. Sivia DS, *Data Analysis - A Bayesian Tutorial*, 1996, Clarendon Press, Oxford
42. Sivia DS, Private communication
43. Weigert G & Baier G, *Astron Astrophys*, 1985, **150**, L18
44. Labeyrie A, *Astron Astrophys*, 1970, **6**, 85
45. Sivia DS, Hamilton WA, Smith GS, Rieker TP & Pynn R, *J Appl Phys*, 1991, **70**, 732
46. Lesslauer W & Blasie JK, *Acta Cryst*, 1971, **A27**, 456
47. Sanyal MK, Sinha SK, Gibaud A, Huang KC, Calvalho BL, Rafailovich M, Sokolov J, Zhao X & Zhao W, *Europhys Letts*, 1993, **21**, 691
48. Sivia DS & Pynn R, SPIE Conference Proc, *Neutron Optical Devices and Applications*, 1992, **1738**, 305
49. Penfold J, Webster JRP, Bucknall DG & Sivia DS, *Colloids and Surfaces A: Physicochem Eng Aspects*, 1994, **86**, 165
50. Lu JR, Li ZX, Smallwood J, Thomas RK & Penfold J, *J Phys Chem*, 1995, **99**, 8233
51. Crowley TL, Lee EM, Simister EA & Thomas RK, *Physica B*, 1991, **173**, 143
52. Henderson JA, Richards RW, Penfold J & Thomas RK, *Macromolecules*, 1993, **26**, 65
53. Moses HE, *Phys Rev*, 1956, **102**, 559
54. Roberts TM, *Physica B*, 1991, **173**, 143
55. Burge RE, Fiddy MA, Greenaway AH & Ross G, *Proc Roy Soc London*, 1976, **A350**, 191
56. Klibanov MV & Sacks PE, *J Math Phys*, 1992 **33**, 3813
57. Klibanov MV & Sacks PE, *J Comput Phys*, 1994, **112**, 273
58. Lipperheide R, Reiss G, Fiedeldey H, Sofianos SA & Leeb H, *Physica B*, 1993, **190**, 377
59. Reiss G & Lipperheide R, *Phys Lett A*, 1994, **196**, 133
60. Lipperheide R, Reiss G, Leeb H, Fiedeldey H & Sofianos SA, *Phys Rev B*, 1995, **51**, 11032
61. Lipperheide R, Fiedeldey H, Leeb H, Reiss G & Sofianos SA, *Physica B*, 1995, **213&214**, 914

62. Reiss G & Lipperheide R, *Phys Rev B*, 1996, **53**, 8157
63. Reiss G, *Physica B*, 1996, **221**, 533
64. Lipperheide R, Reiss G, Leeb H & Sofianos SA, *Physica B*, 1996, **221**, 514
65. Majkrzak CF & Berk NF, *Physica B*, 1996, **221**, 520
66. de Haan VO, van Well AA, Sacks PE, Adenwalla S & Flecher GP, *Physcia B*, 1996, **221**, 524
67. Kramer EJ, *Physcia B*, 1991, **173**, 189
68. Stamm M, *Adv Polym Sci*, 1992, **100**, 357
69. Majkrzak CF, Berk NF, Ankner JF, Satija SK & Russell TP, *SPIE Conf Proc, Neutron Optical Devices and Applications*, 1992, **1738**, 282
70. de Haan VO, van Well AA, Adenwalla S, Felcher GP, *Phys Rev B*, 1995, **52**, 10831
71. Majkrzak CF & Berk NF, *Phys Rev B*, 1995, **52**, 10827
72. Stamm M & Majkrzak CF, *Polymer Preprints*, 1987, **28**, 18
73. Binder K, *J Chem Phys*, 1983, **79**, 6387
74. Fernandez ML, Higgins JS, Penfold J, Ward RC, Shackleton C & Walsh DJ, *Polymer*, 1988, **29**, 1923
75. Russell TP, *Physica B*, 1996, **221**, 267
76. Helfand E & Sapse AM, *J Chem Phys*, 1975, **62**, 1327
77. Shull KR, Mayes AM & Russell TP, *Macromolecules*, 1993, **26**, 3929
78. Guckenbiehl B, Stamm M & Springer T, *Physica B*, 1991, **198**, 127
79. Broseta D, Fredrickson GM, Helfand E & Leibler L, *Macromolecules*, 1990, **23**, 132
80. Schubert DW, Abetz V, Stamm S, Hack T & Siol W, *Macromolecules*, 1995, **28**, 2519
81. Anastasiadis SH, Gancarz I & Koberstien JT, *Macromolecules*, 1988, **21**, 2980
82. Stamm M & Schubert DW, *Annu Rev Mater Sci*, 1995, **25**, 325
83. Müller M, Binder K & Oed W, *J Chem Soc Faraday Trans*, 1995, **91**, 2369
84. Hermes H, Bucknall DG & Higgins JS, *Polymer*, 1996, In press
85. Higgins JS & Oiarzabel L, *ISIS Annual Report*, 1993, A156
86. Fragneto G, Li ZX, Thomas RK, Rennie AR & Penfold J, *J Colloid & Interface Sci*, 1996, **178**, 531
87. Xiao C, Sferrazza M, Jones RAL, Bucknall DG, Penfold J & Webster JRP, submitted to *Phys Rev Lett*, 1996
88. Bucknall DG, Butler S & Higgins JS, Unpublished results, 1996
89. de Gennes PG, *J Chem Phys*, 1971, **55**, 572
90. Doi M & Edwards SJ, *J Chem Soc Faraday Trans 2*, 1978, **74**, 1789, 1802 &1818
91. Russell TP, Deline VR, Dozier WD, Felcher GP, Agrawal G, Wool RP & Mays JW, *Nature*, 1993, **365**, 235
92. Karim A, Mansour A, Felcher GP & Russell TP, *Phys Rev B*, 1990, **42**, 6846
93. Felcher GP, Karim A & Russell TP, *J Non-Cryst Solids*, 1991, **131-133**, 703
94. Stamm M, Hüttenbach S, Reiter G & Springer T, *Europhys Lett*, 1991, **14**, 451
95. Reiter G & Steiner U, *J Phys II*, 1991, **1**, 659
96. Agrawal G, Wool RP, Dozier WD, Felcher GP, Russell TP & Mayes JW, *Macromolecules*, 1994, **27**, 4407
97. Fernandez ML, Higgins JS, Penfold J, Shackleton C & Walsh DJ, *Polymer*, 1990, **31**, 2146
98. Fernandez ML, Higgins JS, Penfold J & Shackleton C, *J Chem Soc: Faraday Trans*, 1991, **87**, 2055
99. Fernandez ML, Higgins JS & Penfold J, *Makrolmol Chem Macromol Symp*, 1992, **62**, 103
100. Sauer BS & Walsh DJ, *Macromolecules*, 1991, **24**, 5948
101. Kunz K & Stamm M, *Makrolmol Chem Macromol Symp*, 1994, **78**, 195
102. Siqueira DF, Schubert DW, Erb V, Stamm M & Ameto JP, *Colloid Polym Sci*, 1995, **273** 1041
103. Kunz K & Stamm M, *Macromolecules*, 1996, **29**, 2548
104. Chaturverdi U, Steiner U, Krausch G & Klein J, *Phys Rev Lett*, 1989, **63**, 616
105. Guckenbiehl G, *PhD Thesis*, 1993, University of Mainz
106. Puri S & Binder K, *Phys Rev B*, 1991, **17**, 9375
107. Whitlow SJ & Wool RP, *Macromolecules*, 1989, **22**, 2648
108. Coulon G, Russell TP, Deline VR & Green PF, *Macromolecules*, 1989, **22**, 2581
109. Bucknall DG, Fernandez ML & Higgins JS, *Faraday Dicuss*, 1994, **98**, 19
110. Brochard-Wyart F & de Gennes PG, *Makromol Chem Macromol Symp*, 1990, **40**, 167
111. Jones RAL & Sivaniah E, *ISIS Annual Report RAL-TR-95-050*, 1995, II, A382
112. Jones RAL & Sivaniah E, *ISIS Annual Report, RAL-TR-96*, 1996, II, A440
113. Bhatia QS, Pan DH & Koberstein JT, *Macromolecules*, 1988, **21**, 2166
114. Jones RAL, Norton LJ, Kramer EJ, Composto RJ, Stein RS, Russell TP, Mansour A, Karim A, Felcher GP, Raifailovich MH, Sokolov J, Zhao X & Schwarz SA, *Europhys Lett*, 1990, **12**, 41

115. Hariharan A & Kumar SK, *Macromolecules*, 1991, **24**, 4909
116. Zhao X, Zhao W, Sokolov J, Rafailovich MH, Schwarz SA, Wikens BJ, Jones RAL & Kramer EJ, *Macromolecules*, 1991, **24**, 5991
117. Budkowski A, Steiner U & Klein J, *J Chem Phys*, 1992, **97**, 5229
118. Steiner U, Klein J, Eiser E, Budkowski A & Fetters LJ, *Science*, 1992, **258**, 1126
119. Zhao X, Zhao W, Zheng X, Rafailovich MH, Sokolov J, Schwarz SA, Pudensi MAA, Russell TP, Kumar SK & Fetters LJ, *Phys Rev Lett*, 1992, **69**, 776
120. Bruder F & Brenn R, *Europhys Lett*, 1993, **22**, 707
121. Steiner U, Klein J & Fetters LJ, *Phys Rev Lett*, 1994, **72**, 1498
122. Geoghegan M, Jones RAL, Payne RS, Sakellariou P, Clough AS & Penfold J, *Polymer*, 1994, **35**, 2019
123. Guckenbiehl G, Stamm M & Springer T, *Colloid & Surf A*, 1994, **86**, 311
124. Elman JF, Johs BD, Long TE & Koberstein JT, *Macromolcules*, 1994, **27**, 5341
125. Geoghegan M, Jones RAL & Clough AS, *J Chem Phys*, 1995, **103**, 2719
126. Norton LJ, Kramer EJ, Bates FS, Gehlsen MD, Jones RAL, Karim A, Felcher GP & Kleb R, *Macromolecules*, 1995, **28**, 8621
127. Hopkinson I, Kiff FT, Richards RW, Affrossman S, Hartshorne M, Pethrick RA, Munro H & Webster JRP, *Macromolecules*, 1995, **28**, 627
128. Kunz K, Stamm M, Harthorne M & Affrossman S, *Acta Polymer*, 1996, **47**, 234
129. Nakanishi H & Fisher ME, *J Chem Phys*, 1983, **78**, 3279
130. Nakanishi H & Pincus P, *J Chem Phys*, 1983, **79**, 997
131. Schmidt L & Binder K, *J Phys (Paris)*, 1985, **46**, 1631
132. Mon KK, Binder K & Landau DP, *Phys Rev B*, 1987 **35**, 3683
133. Cohen SM & Muthukumar M, *J Chem Phys*, 1989, **90**, 5749
134. Carmesin I & Noolandi J, *Macromolecules*, 1989, **22**, 1689
135. Shull KR & Kramer EJ, *Macromolecules*, 1990, **23**, 4769
136. Wang JS & Binder K, *J Chem Phys*, 1991, **94**, 8537
137. Chen ZY, Noolandi J & Izzo D, *Phys Rev Lett*, 1991, **66**, 727
138. Cifra P, Karasz FE & MacKnight WJ, *Macromolecules*, 1992, **25**, 4895
139. Jerry RA & Nauman EB, *Phys Lett A*, 1992, **167**, 198
140. Puri S & Binder K, *Z Phys B*, 1992, **86**, 263
141. Jones RAL, *Phys Rev E*, 1993, **47**, 1437
142. Hariharan A, Kumar SK & Russell TP, *J Chem Phys*, 1993, **99**, 4041
143. Cifra P, Bruder F & Brenn R, *J Chem Phys*, 1993, **99**, 4121
144. Genzer J, Faldi A & Composto RJ, *Phys Rev E*, 1994, **50**, 2373
145. Jones RAL, *Polymer*, 1994, **35**, 2160
146. Brown G, Chakrabarti A & Marko JF, *Phys Rev E*, 1994, **50**, 1674
147. Krausch G, Dai CA, Kramer EJ, Marko JF, Bates FS & Wiltzius P, *Macromolecules*, 1993, **26**, 5566
148. Krausch G, Dai CA, Kramer EJ & Bates FS, *Phys Rev Lett*, 1993, **71**, 3669
149. Kim E, Krausch G, Kramer EJ & Osby JO, *Macromolecules*, 1994, **27**, 5927
150. Bruder F & Brenn R, *Ohys Rev Lett*, 1992, **69**, 624
151. Krausch G, Mlyner J, Straub W, Brenn R & Marko JF, *Europhys Lett*, 1994, **28**, 323
152. Geoghegan M, Jones RAL, Clough AS & Penfold J, *J Polym Sci B: Polym Phys*, 1995, **33**, 1307
153. Jones RAL, Norton LJ, Shull KR, Kramer EJ, Felcher GP, Karim A & Fetters LJ, *Macromolecules*, 1992, **25**, 2359
154. Shull KR & Winey KI, *Macromolecules*,1992, **25**, 2637
155. Clarke CJ, Jones RAL, Edwards JL, Clough AS & Penfold J, *Polymer*, 1994, **35**, 4065
156. Hopkinson I, Kiff FT, Richards RW, Bucknall DG & Clough AS, *Polymer*, In press
157. Fleer GJ, Cohen-Stuart MA, Scheutjens JMHM, Cosgrove T & Vincent B, *Polymers at Interfaces*, 1993, Chapman & Hall, London
158. Molau GE in *Block Copolymers*, Ed Aggrawal SL, 1970, Plenum Press, New York, pg79
159. Riess G, Periard J & Jolivet Y, *Angew Chem Int Ed Engl*, 1972, **11**, 339
160. Heikens D & Barentsen WM, *Polymer*, 1977, **18**, 70
161. Paul DR in *Polymer Blends*, Eds Paul DR & Newmann S, 1978, Academic Press, Vol 2, pg 35
162. Fayt R, Jérôme R & Teyssié Ph, *J Polym Sci Polym Lett*, 1986, **24**, 25
163. Ouhadi T, Fayt R, Jérôme R & Teyssié Ph, *Polym Commun*, 1986, **27**, 212
164. Anastasiadis SH, Gancarz I & Koberstein JT, *Macromolecules*, 1989, **22**, 1449
165. Brown HR, *Macromolecules*, 1989, **22**, 2859

166. Creton C, Kramer, EJ & Hadziioannou G, *Macromolecules*, 1991, **24**, 1846
167. Shull KR, Kellock AJ, Deline VR & MacDonald SA, *J Phys Chem*, 1992, **97**, 2095
168. Bucknall DG, Higgins JS & Rostami S, *Polymer*, 1992, **33**, 4419
169. Oliver SL, Titman JJ, Bucknall DG & Higgins JS, *paper in preparation*
170. Hermes HE, Higgins JS, Bucknall DG, *paper in preparation*
171. Vilgis TA & Noolandi J, *Macromolecules*, 1990, **23**, 2941
172. Noolandi J & Hong KM, *Macromolecules*, 1982, **15**, 482
173. Fayt R, Jérôme R & Teyssié Ph, *Makromol Chem*, 1986, **187**, 837
174. Dai KH, Norton LJ & Kramer EJ, *Macromolecules*, 1994, **27**, 1949
175. Russell TP, Anastasiadis SH, Menelle A, Felcher GP & Satija SK, *Macromolecules*, 1991, **24**, 1575
176. Russell TP, Menelle A, Hamilton WA, Smith GS, Satija SK & Majkrzak CF, *Macromolecules*, 1991, **24**, 5721
177. Leibler L, *Makromol Chem Macromol Symp*, 1988, **16**, 1
178. Noolandi J, *Polym Eng Sci*, 1984, **24**, 70 & Noolandi J & Hong KM, *Macromolecules*, 1984, **17**, 1531
179. Semenov AN, *Macromolecules*, 1992, **25**, 4967
180. Bucknall DG, *PhD Thesis*, Imperial College, University of London, 1991
181. Kinning DJ, Winey KI & Thomas EL, *Macromolecules*, 1988, **21**, 3502
182. Shull KR, Kramer EJ, Hadziioannou & Tang W, *Macromolecules*, 1990, **23**, 4780
183. Goodman I, Ed, *Developments in Block Copolymers I*, 1985, Applied Science, New York
184. Fredrickson GH, *Macromolecules*, 1987, **20**, 2535
185. Shull KR, *Macromolecules*, 1992, **25**, 2122
186. Russell TP, Coulon G, Deline VR & Miller DC, *Macromolecules*, 1989, **22**, 4600
187. Anastasiadis SH, Russell TP, Satija SK & Majkrzak CF, *Phys Rev Lett*, 1989, **62**, 1852
188. Menelle A, Russell TP, Anastasiadis SH, Satija SK & Majkrzak CF, *Phys Rev Lett*, 1992, **68**, 67
189. Mayes AM & Russell TP, *J de Phys IV Colloq C8*, 1993, **3**, 41
190. Mayes AM, Johnson RD, Russell TP, Smith SD, Satija SK & Majkrzak CF, *Macromolecules*, 1993, **26**, 1047
191. Russell TP, Lambooy P, Kellogg GJ & Mayes AM, *Physica B*, 1995, **213/214**, 22
192. Kellogg GJ, Walton DG, Mayes AM, Lambooy P, Russell TP, Gallagher PD & Satija SK, *Phys Rev Lett*, 1996, **76**, 2503
193. Lambooy P, Russell TP, Kellogg GJ, Mayes AM, Gallagher PD & Satija SK, *Phys Rev Lett*, 1994, **72**, 2899
194. Lin H, Steyerl A, Satija SK, Karim A & Russell TP, *Macromolecules*, 1995, **28**, 1470
195. Mayes AM, Russell TP, Satija SK & Majkrzak CF, *Macromolecules*, 1992, **25**, 6523
196. Shull KR, *Macromolecules*, 1993, **26**, 2346
197. Fredrickson GH, *Macromolecules*, 1986, **85**, 5306
198. Fredrickson GH, *J Chem Phys*, 1987, **87**, 697
199. Leibler L, *Macromolecules*, 1980, **13**, 1602
200. Hayter JB & Mook HA, *J Appl Cryst*, 1989, **22**, 35
201. Koneripalli N, Singh N, Levicky R, Bates FS, Gallagher PD & Satija SK, *Macromolecules*, 1995, **28**, 2897
202. Shull KR, *J Chem Phys*, 1991, **94**, 5723
203. Walton DG, Kellogg GJ, Mayes AM, Lambooy P & Russell TP, *Macromolecules*, 1994, **27**, 6225